*J Neurophysiol* 91: 1963–1980, 2004.
First published December 31, 2003; 10.1152/jn.00924.2003.

# A Model of Reverse Spike Frequency Adaptation and Repetitive Firing of Subthalamic Nucleus Neurons

**Charles J. Wilson,[1] Angela Weyrick,[1] David Terman,[2] Nicholas E. Hallworth,[3] and Mark D. Bevan[3]**
[1]*Department of Biology, University of Texas at San Antonio, San Antonio, Texas 78249;* [2]*Department of Mathematics, Ohio State University, Columbus, Ohio 43210; and* [3]*Department of Physiology, Northwestern University Feinberg School of Medicine, Chicago, Illinois 60611*

Submitted 22 September 2003; accepted in final form 29 December 2003

**Wilson, Charles J., Angela Weyrick, David Terman, Nicholas E. Hallworth, and Mark D. Bevan.** A model of reverse spike frequency adaptation and repetitive firing of subthalamic nucleus neurons. *J Neurophysiol* 91: 1963–1980, 2004. First published December 31, 2003; 10.1152/jn.00924.2003. Subthalamic nucleus neurons exhibit reverse spike-frequency adaptation. This occurs only at firing rates of 20–50 spikes/s and higher. Over this same frequency range, there is an increase in the steady-state frequency–intensity (*F–I*) curve's slope (the secondary range). Specific blockade of high-voltage activated calcium currents reduced the *F–I* curve slope and reverse adaptation. Blockade of calcium-dependent potassium current enhanced secondary range firing. A simple model that exhibited these properties used spike-triggered conductances similar to those in subthalamic neurons. It showed: *1*) Nonaccumulating spike afterhyperpolarizations produce positively accelerating *F–I* curves and spike-frequency adaptation that is complete after the second spike. *2*) Combinations of accumulating aftercurrents result in a linear *F–I* curve, whose slope depends on the relative contributions of inward and outward currents. Spike-frequency adaptation can be gradual. *3*) With both accumulating and nonaccumulating aftercurrents, primary and secondary ranges will be present in the *F–I* curve. The slope of the primary range is determined by the nonaccumulating conductance; the accumulating conductances govern the secondary range. The transition is determined by the relative strengths of accumulating and nonaccumulating currents. *4*) Spike-threshold accommodation contributes to the secondary range, reducing its slope at high firing rates. Threshold accommodation can stabilize firing when inward aftercurrents exceed outward ones. *5*) Steady-state reverse adaptation results when accumulated inward aftercurrents exceed outward ones. This requires spike-threshold accommodation. Transient speedup arises when inward currents are smaller than outward ones at steady state, but accumulate more rapidly. *6*) The same mechanisms alter firing in response to irregular patterns of synaptic conductances, as cell excitability fluctuates with changes in firing rate.

## INTRODUCTION

Early intracellular recording studies of spinal cord motoneurons driven to fire by application of intracellular current pulses revealed a complex relationship between applied current and firing frequency (e.g., Granit et al. 1963). When applied currents were low, neuronal firing rate increased linearly with injected current. At higher rates the slope of the relationship between frequency and current (*F–I* curve) increased dramatically, and this steeper region of the *F–I* curve was called the secondary range. At higher values of current, where the neuron approached its highest possible firing rate, the slope of the *F–I* curve usually was reduced, and this region was sometimes called the tertiary range (Schwindt 1973). In motoneurons, the slopes of the primary and secondary ranges decrease over time during sustained activity, which has been attributed to spike-frequency adaptation (Kernell 1965).

A variety of other neurons show firing characteristics similar to those of motoneurons, but most neurons in the brain whose *F–I* curves have been studied in detail have had a simpler relationship between current and frequency. There have been many studies of the neocortical pyramidal cell, for example, which show a nearly linear steady-state *F–I* curve over most of its firing range, with only a decrease in slope seen near maximal firing rates (similar to the tertiary range of motoneurons) (e.g., Stafstrom et al. 1984).

Recently, we observed that neurons of the subthalamic nucleus (STN) neurons exhibit a sigmoidal *F–I* curve, similar to that seen for motoneurons (Bevan and Wilson 1999; Hallworth et al. 2003). The existence of a secondary range of the *F–I* curve in STN neurons may be functionally significant because it suggests that the neurons may become more sensitive to synaptic input when already excited and firing at a moderately high rate. The range of firing rates over which STN neurons exhibit this enhanced sensitivity corresponds roughly to that obtained during bursts of firing that can be observed in those neurons during movements (Cheruel et al. 1996; Wichmann et al. 1994). The mechanism of the enhancement of sensitivity has not been explored in detail, but it occurs in the same frequency range as another unusual feature of these neurons, a reverse spike-frequency adaptation or speedup of firing over the first 10–50 action potentials of repetitive firing. This speedup is not seen when the cell is firing in the primary range, but is prominent at frequencies corresponding to the steepest part of the secondary range (Hallworth et al. 2003).

Subthalamic neurons exhibit a variety of voltage-sensitive conductances, some activated in the subthreshold membrane potential trajectory between action potentials and some activated at voltages visited by the membrane potential only during action potentials (Baranauskas et al. 2003; Beurrier et al. 1999; Bevan and Wilson 1999; Hallworth et al. 2003; Song et al. 2000; Wigmore and Lacey 2000). In the period after the rapid repolarization of the membrane after an action potential, those high-voltage activated (HVA) conductances may be strongly activated by the brief depolarization, then deactivate at their characteristic rates, relatively unaffected by the subthreshold

Address for reprint requests and other correspondence: C. J. Wilson, Department of Biology, University of Texas at San Antonio, 6900 N. Loop 1604 W., San Antonio, TX 78249.

The costs of publication of this article were defrayed in part by the payment of page charges. The article must therefore be hereby marked "*advertisement*" in accordance with 18 U.S.C. Section 1734 solely to indicate this fact.

trajectory of the membrane potential during the interspike interval (ISI). Thus these conductances can be thought of as simple functions of time since an action potential. STN neurons are fast-spiking cells, with powerful spike-triggered potassium currents responsible for their rapid repolarization and the early component of the afterhyperpolarization (AHP) (Baranauskas et al. 2003; Wigmore and Lacey 2000). In addition, HVA calcium currents are triggered during the action potential, but deactivate slowly enough for them to long outlive the action potential. Calcium imaging experiments on spontaneously firing STN neurons show that the peak calcium current occurs during the spike AHP, and calcium entry into the cell after a single action potential is not complete until several milliseconds after the action potential is over (Hallworth et al. 2003). Calcium entry triggers a still slower conductance, the apamin-sensitive calcium-dependent potassium current, which is largely responsible for the slow component of the spike AHP (Hallworth et al. 2003). In addition to these 3 major sets of spike-triggered currents, there is a persistent sodium current active over most of the subthreshold interspike trajectory of the membrane potential (Beurrier et al. 2000; Bevan and Wilson 1999; Do and Bean 2003). Both spike-triggered and subthreshold currents have been implicated in the secondary range firing of motoneurons (e.g., Schwindt and Crill 1982) and are also likely candidates for controlling the repetitive firing of STN neurons. Here we examine the repetitive firing of subthalamic cells, its dependency on spike-triggered calcium current and calcium-dependent potassium current, and offer a model for reverse spike-frequency adaptation and the generation of their sigmoidal *F–I* curves.

## METHODS

### *Experimental*

The intracellular recordings reported here are from data gathered in the course of a recent study (Hallworth et al. 2003), and the methods used are described in detail there. Brain slices were prepared from 43 16- to 30-day-old Sprague–Dawley rats, anesthetized with a mixture of ketamine and xylazine, and perfused transcardially with 10–40 ml of oxygenated ice-cold modified artificial cerebrospinal fluid (ACSF) containing (in mM): 230 sucrose, 2.5 KCl, 1.25 $Na_2HPO_4$, 0.5 $CaCl_2$, 10 $MgSO_4$, and 10 glucose. Slices containing the STN neurons were cut at a thickness of 300 $\mu$m and maintained at room temperature, in oxygenated ACSF containing (in mM): 126 NaCl, 2.5 KCl, 1.25 $Na_2HPO_4$, 2 $CaCl_2$, 2 $MgSO_4$, and 10 glucose.

Single slices were transferred to the recording chamber and perfused continuously (2–3 ml/min) with oxygenated ACSF at 37°C. Recording pipettes were filled with a solution containing (in mM): 134.1 K-$MeSO_4$, 0.9 KCl, 3.6 NaCl, 1 $MgCl_2 \cdot 6H_2O$, 10 HEPES, 0.1 $Na_4$EGTA, 0.4 $Na_3$GTP, and 2 $Mg_{1.5}$ATP. Gramicidin was added to the pipette solution at a concentration of 20 $\mu$g/ml less than 1 h before seal formation was attempted. The resistance of filled pipettes was between 2.5 and 5 M$\Omega$. Perforated somatic recordings were made under visual control (using IR-infragradient interference optics). Junction potentials were not corrected in the perforated configuration. Deliberate or accidental establishment of the whole cell configuration was recognized by a sudden decrease in series resistance, an increase in the amplitude of recorded action potentials, and a 5- to 7-mV offset in membrane potential. The latter was attributed to the dialysis of the intracellular compartment with the electrode solution and the value of the offset was similar to the empirically determined or theoretically calculated junction potential between the electrode solution and the external media (Bevan and Wilson 1999; Bevan et al. 2000). Fast capacitive transients of the pipette were nulled on-line; there was no on-line compensation of series resistance or whole cell capacitance. Voltage errors ascribed to the electrode resistance were removed from the traces off-line during analysis.

Drugs were diluted in ACSF and bath-applied. Fast synaptic transmission was blocked by the continuous application of 50 $\mu$M D-(−)-2-amino-5-phosphonopentanoic acid (APV), 20 $\mu$M 6,7-dinitroquinoxaline-2,3-dione (DNQX), and 20 $\mu$M SR 95531 hydrobromide (GABAzine) (all from Tocris, Ellisville, MO) so that the action of SK and $Ca_v$ channel drugs on intrinsic properties could be studied in isolation from effects on synaptic transmission. Nifedipine (5 $\mu$M, Tocris), $\omega$-conotoxin-GVIA (1 $\mu$M, Sigma, St. Louis, MO), and apamin (1 pM–100 nM, Sigma) were used to block calcium and calcium-dependent potassium channels.

### *Modeling*

Computer simulations were performed using xppaut (B. Ermentrout, Univ. of Pittsburgh). For the class of models without explicit action potential currents, we used Runge–Kutta integration and a time step of 0.05 ms. The model neurons used for this class of simulation consisted of a leak conductance, and 1–3 voltage-insensitive conductances. The current balance equation for the cells was $dv/dt = (I_{app} + g_L(v - v_L) + g_f(v - v_o) + g_m(v - v_i) + g_s(v - v_o))/C$, in which $I_{app}$ is the injected current; $v_L$ is the reversal potential for the leak current; $g_f$, $g_m$, and $g_s$ are the fast, medium, and slow afterconductances; and $v_o$ and $v_i$ are the reversal potentials for outward and inward aftercurrents, respectively. Capacitance was taken as 1 $\mu F/cm^2$, and all currents were normalized to the membrane surface area. At the time of an action potential, each of the spike-triggered conductances was incremented by a proportion $\delta$ of the maximal conductance $\bar{g}$. They each would then decay exponentially at a rate determined by a time constant $\tau$

$$g_f = \bar{g}_f \delta_f \exp(-t/\tau_f)$$

$$g_m = \bar{g}_m \delta_m \exp(-t/\tau_m)$$

$$g_s = \bar{g}_s \delta_s \exp(-t/\tau_s)$$

Accumulating conductances were characterized by small values of the per-spike increment $\delta$, so that they would not exceed their maximal values. Nonaccumulating conductances were adjusted so that each spike reset them to their maximal values ($\delta = 1$).

The action potential occurred whenever the membrane potential exceeded a voltage threshold, which could be fixed, or would also be incremented by each action potential and decay exponentially in time after a spike. All conductances and currents were normalized to the surface area.

For the more realistic simulations, the QualRk integration method (an adaptive-step 4th-order version of Runge–Kutta) was used, with a tolerance of 0.001 and a time step of 0.2 ms. The subthalamic nucleus neuron was represented as a single compartment, but the intracellular compartment consisted of 40 concentric shells for purposes of representing calcium diffusion [simplified from that used in Wilson and Callaway (2000)]. Calcium disposition was represented as a nonsaturable pump on the cell membrane characterized by a single pump rate $k_{Ca}$. A nonsaturable buffer was present in all compartments, leading to a constant ratio $\beta$ of free to buffered calcium, and diffusion from one compartment to the next occurred according to an effective diffusion constant. Thus diffusion into and from the jth compartment was governed by the diffusion equation

$$Ca[j]' = D_{app}/(v[j]\Delta r)((Ca[j-1] - Ca[j])sa[j] - (Ca[j] - Ca[j+1])sa[j+1])$$

in which $D_{app}$ is the effective diffusion coefficient of free calcium, $\Delta r$ is the shell thickness, Ca[j] is the concentration of calcium in the jth

compartment, sa[j] is the surface area of the outer surface of the jth shell, and v[j] is the volume of the jth shell.

For the outermost shell

$$Ca[0]' = \beta(sa[0]/v[0])[-I_{Ca}/zF - (Ca[0]k_{Ca}) - D_{app}sa[1]/(v[0]\Delta r)(Ca[0] - Ca[1])]$$

in which $I_{Ca}$ is the calcium current, z is the valence of calcium, F is Faraday's constant, $\beta$ is the buffering ratio, and $k_{Ca}$ is the pump rate as described above. Calcium current and fast AHP current were noninactivating and controlled by activation variables c and n, which evolved according to the following equations

$$I_K = \bar{g}_K n^4(v - v_K)$$

$$I_{Ca} = \bar{g}_{Ca} c(v - v_{Ca})$$

$$n' = \phi_n[n_\infty(v) - n]/\tau_n(v)$$

$$c' = \phi_c[c_\infty(v) - c]/\tau_c(v)$$

$$n_\infty(v) = 1/\{1 + \exp[(v - vh_n)/vs_n]\}$$

$$c_\infty(v) = 1/\{1 + \exp[(v - vh_c)/vs_c]\}$$

$$\tau_n(v) = \tau_n^0 + \tau_n^1/\{1 + \exp[(v - vh_n^\tau)/vs_n^\tau]\}$$

$$\tau_c(v) = \tau_c^0 + \tau_c^1/\{1 + \exp[(v - vh_c^\tau)/vs_c^\tau]\}$$

in which $\phi$ values are temperature variables that control the rate of activation and deactivation in a voltage-independent fashion, $vh_n$ and $vh_c$ are half-activation voltages, and $vs_n$ and $vs_c$ are slope factors for the voltage dependency of activation. Time constants are sigmoidal functions of voltage, and $vh_n^\tau$, $vh_c^\tau$, $vs_n^\tau$, and $vs_c^\tau$ are the half-maximal and slope factor parameters for the voltage dependency of activation and deactivation.

Activation and deactivation of the sodium current was treated as instantaneous, with a voltage sensitivity given by

$$I_{Na} = \bar{g}_{Na} m^3 h(v - v_{Na})$$

$$m(v) = 1/\{1 + \exp[(v - vh_m)/vs_m]\}$$

Inactivation of the sodium current was controlled by an inactivation variable h

$$h' = \phi_h[h_\infty(v) - h]/\tau_h(v)$$

$$h_\infty(v) = 1/\{1 + \exp[(v - vh_h)/vs_h]\}$$

$$\tau_h(v) = \tau_h^0 + \tau_h^1/\{1 + \exp[(v - vh_h^\tau)/vs_h^\tau]\}$$

The calcium-dependent $K^+$ current depended on calcium concentration in the outermost shell and the half-activation concentration of calcium ($k_1$)

$$I_{AHP} = \bar{g}_{AHP}(v - v_K)\{Ca[0]/(Ca[0] + k_1)\}$$

Typical parameters (parameters used in Figs. 7 and 8) are given in Table 1.

TABLE 1. *Parameters and typical values for the single compartment*

| Parameter | Value | Parameter | Value |
|---|---|---|---|
| $\bar{g}_L$ | 2.25 mS/cm$^2$ | $vh_n$ | −32 mV |
| $\bar{g}_{Ca}$ | 5 mS/cm$^2$ | $vh_c$ | −20 mV |
| $\bar{g}_{Na}$ | 80 mS/cm$^2$ | $vh_m$ | −30 mV |
| $\bar{g}_{AHP}$ | 2.75 mS/cm$^2$ | $vh_h$ | −39 mV |
| $\bar{g}_K$ | 30 mS/cm$^2$ | $vs_n$ | 8 mV |
| $v_L$ | −60 mV | $vs_c$ | 8 mV |
| $v_{Ca}$ | 140 mV | $vs_m$ | 15 mV |
| $v_{Na}$ | 55 mV | $vs_h$ | 3.1 mV |
| $v_K$ | −80 mV | $vh_n^\tau$ | −80 mV |
| $\phi_n$ | 1.25 | $vh_c^\tau$ | −80 mV |
| $\phi_c$ | 0.08 | $vh_h^\tau$ | −57 mV |
| $\phi_h$ | 1.25 | $vs_n^\tau$ | 26 mV |
| $\tau_n^0$ | 1 ms | $vs_c^\tau$ | 26 mV |
| $\tau_n^1$ | 100 ms | $vs_h^\tau$ | 5 mV |
| $\tau_c^0$ | 1 ms | $k_1$ | 0.2 $\mu$M |
| $\tau_c^1$ | 10 ms | $\beta$ | 0.001 |
| $\tau_h^0$ | 1.5 ms | $D_{app}$ | 0.02 $\mu$m/ms |
| $\tau_h^1$ | 1,500 ms | r | 8 $\mu$m |
| | | C | 1 $\mu$F/cm$^2$ |

## RESULTS

### *Speedup and sigmoidal F–I curve in subthalamic neurons*

The experimental data used here were from 11 cells recorded before and after application of nifedipine (5 $\mu$M), 17 cells recorded before and after application of apamin (3 given 10 nM, 14 given 100 nM), and 20 cells recorded before and after application of $\omega$-conotoxin-GVIA (1 $\mu$M). These are the same cells used in Hallworth et al. (2003), and the basic results were reported there, but some additional analysis is reported here. Current pulses of 500 ms were applied by the recording electrode. Currents steps increased by 20 pA intervals, starting from 0 and ending at least 40 pA beyond the maximal rate for the cell. An example of a cell showing repetitive firing before application of any drug, showing the repetitive firing of a subthalamic neuron, is shown in Fig. 1, *A–E*. As we previously reported (Bevan and Wilson 1999), subthalamic cells are spontaneous pacemakers, and fire at a low steady rate in the absence of applied current. Hyperpolarization of the cells produced continuous decreases in their firing rate with no definite minimum rate of firing. Depolarizing current pulses produced continuous increases in firing rate. At low rates, most cells showed a small degree of spike-frequency adaptation (example trace and rate vs. spike number curve marked 60 pA). For these rates, the steady-state *F–I* curve (as estimated by the average rate during the pulse) had an approximately constant and low slope, with frequency increasing by about 20 spikes/s per 100 pA (Fig. 1*C*). A comparison of the frequency calculated from the first interval and a mean frequency calculated over all spikes during a 500-ms pulse revealed only a small amount of spike-frequency adaptation at these low rates, which correspond to the primary firing range. At rates corresponding to the high slope region of the *F–I* curve (Fig. 1*A*, *trace* marked 180 pA and Fig. 1*B*, curves 160, 200, and 280 pA), firing frequency increased over the first part of the train, then leveled off or decreased slightly, but usually ended the train at a higher rate than that for the first ISI. The *F–I* curve calculated for the first ISI over the secondary range was nearly linear and had nearly the same slope as that of the primary range. The mean rate in the secondary range deviated from the rate calculated from the first interval, as expected from the rate speedup seen in the rate versus spike number graphs. At high firing rates, speedup continued to occur at the beginning of the train, but was less effective at raising the mean firing rate because of an apparent saturation of firing (Fig. 1*B*). At these higher rates, firing failed before the termination of the current pulse (not shown). During the train of action potentials, the spike threshold increased, and the membrane potential achieved at the depth of the spike AHP became less negative.

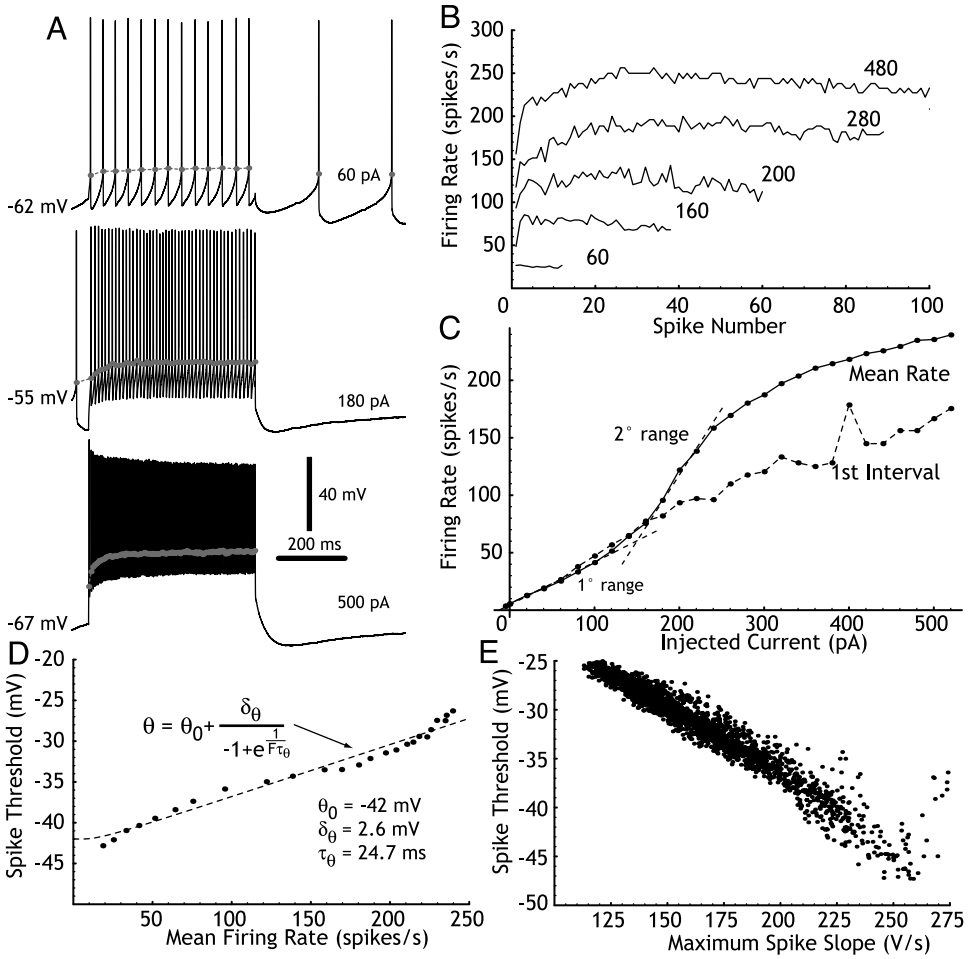


FIG. 1. Properties of repetitive firing of subthalamic neurons in response to constant current pulses. *A*: responses of a subthalamic cell to current pulses. Spike threshold, defined as the point at which dV/dt > 10 mV/ms is marked for each spike as a gray dot. *B*: firing rate evolution during repetitive firing evoked by constant current pulses. Each curve is labeled with the current (in pA) that evoked the firing. *C*: the *F*/*I* curve for the same cell, over a range of current pulse amplitudes. The *F*/*I* curves were calculated for the first interspike interval and the mean over the entire pulse. The primary and secondary ranges are marked by dotted lines. *D*: the steady state spike threshold (threshold for the last spike) for the pulses used in the *F*/*I* curve in *C*, plotted against the mean firing rate. The best fitting curve for spike-triggered changes in spike threshold (as used in the simple model) is superimposed. *E*: spike threshold plotted against maximum spike slope for all the spikes used to calculate the *F*/*I* curves for this cell. Note that changes in spike threshold are closely related to changes in maximum spike slope.

The change in spike threshold is apparent in the *traces* in Fig. 1*A*, in which the threshold is indicated by a gray dot at the point that the temporal change in membrane potential exceeded 10 mV/ms. The threshold (and depth of AHP) change caused the mean value of the subthreshold membrane potential trajectory during the spike train to increase during the spike train. Threshold changes achieved steady-state values over the first 200 ms of spike trains at all current levels. The steady-state threshold values are plotted against the mean firing rate in Fig. 1*D*. A curve showing the best fit to the data for an expected value of threshold based on a simple model, in which each spike causes an increment in threshold $\delta_\theta$ over a baseline threshold $\theta_0$, and threshold relaxes exponentially back to the baseline with time constant $\tau_\theta$. This simple model does not capture all the changes in threshold and is especially inaccurate at low frequencies, probably because threshold changes arise from channel activation and inactivation elicited by subthreshold membrane potential changes, as well as by the larger deviations in membrane potential associated with action potentials. Over much of the range of high-frequency firing, it makes a reasonable approximation, however. Much of the change in threshold could be accounted for by accumulation of sodium channel inactivation. This is shown in Fig. 1*E*, in which sodium channel activation for each action potential is estimated by the maximum slope of the action potential, and plotted against threshold. The strong negative correlation between peak spike slope and spike threshold indicates that both of them are controlled by the same underlying variable, sodium channel availability at the time of the action potential.

Of the 49 cells for which predrug measurements were available, 37 exhibited speedup, as illustrated in Fig. 1, 5 showed no net change in rate over the course of 500-ms current pulses in the secondary range, and 7 showed no speedup, but rather a small degree of spike-frequency adaptation. All but 4 of the cells had clearly sigmoidal mean rate *F–I* curves.

### *The effect of apamin blockade of the slow AHP*

Blockade of the slow AHP was performed using bath application of apamin (10 or 100 nM) to block SK channels present on the membrane of STN neurons ($n = 17$). This was previously shown to increase driven firing rates of STN neurons in slices (Bevan and Wilson 1999; Hallworth et al. 2003). This treatment consistently caused increases in driven firing rates of subthalamic cells, and in 14 of 17 cells there was a clear leftward shift in the *F–I* curve, as shown in Fig. 2, *A–C*. Of 17 neurons studied with apamin, 12 showed clear speedup of firing in control recordings. All 12 continued to show a strong firing speedup after apamin treatment, but at lower current levels than previously required. The maximum firing rate achieved at high current levels was the same for apamin versus control firing. Apamin also had no consistent effect on the *F–I* curve calculated from the first interspike interval.

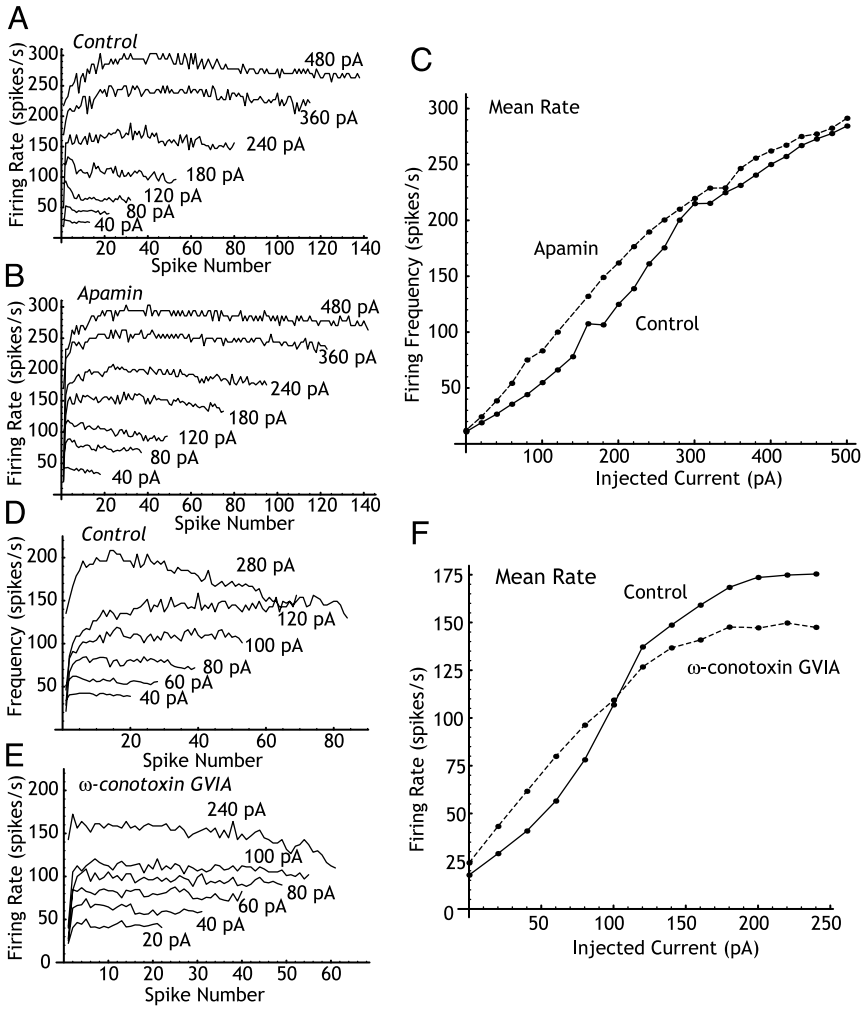


FIG. 2. Effects of apamin and ω-conotoxin-GVIA blockade of SK channels on repetitive firing and *F–I* curves for STN neurons. Instantaneous firing rate evolution during current pulses before application of apamin (*A*) after apamin treatment (*B*). *C*: *F–I* curves for mean firing rate over the entire period of driven firing in the control and apamin-containing media. *D–F*: effects of ω-conotoxin-GVIA blockade of $Ca_v2.2$ calcium channels on repetitive firing and *F–I* curves for STN neurons. Evolution of instantaneous firing rate during current pulses before application of conotoxin (*D*) and after treatment with conotoxin (*E*). *F*: mean firing rate *F–I* curves for conotoxin and control.

*Blockade of specific calcium channels with nifedipine or ω-conotoxin-GVIA*

Cav1.2–1.3 (L-type) channels were blocked by addition of 5 μM nifedipine to the superfusion medium, and recordings were all made at least 10 min after addition of nifedipine. Of these cells, 8 exhibited firing speedup in control solution and 3 did not. In these 8 cells, nifedipine reduced or abolished speedup in 7. Nifedipine did not change the overall shape of the *F–I* curve, but decreased the maximal rate in 7 of 11 cells. There was no significant reduction in the spike AHP, suggesting that calcium entry driving the apamin-sensitive current was still mostly or completely intact.

Addition of ω-conotoxin-GVIA (1 μM) to the superfusing solution was tested in 20 neurons, including 15 that showed clear speedup in the secondary range and 5 that did not. Among the 15 cells that showed speedup, it was abolished or substantially reduced in 14, with one cell showing no change. The maximum firing rate at high current levels was reduced in 17 of 20 neurons tested, and 13 of 20 cells showed a flattening in the shape of the *F–I* curve as illustrated in Fig. 2. This consists of both a decrease in the maximal rate and an increase in the rate at low currents, so that the *F–I* curve was flattened. The main difference between the effects of nifedipine and those of conotoxin was apparent at lower currents, in that the latter caused an increase in firing rate at low frequencies as well as a decrease in the maximal rate. Figure 2, *D–F* shows these results for an example cell treated with ω-conotoxin-GVIA.

*A model using spike-triggered conductances*

Because our experimental evidence suggested that calcium currents involved in driven firing were mostly HVA currents triggered by action potentials (Hallworth et al. 2003), we first constructed a simplified model of the STN neurons based on conductances activated at voltages achieved only during the action potential. The simplest of these is an abstract neuron model based on an adaptation of the integrate-and-fire neuron using a fixed spike threshold and conductances generated only by action potentials. The action potential itself is not represented in the model, but when the membrane potential crosses spike threshold, it triggers one or more exponentially decaying conductances characterized only by their initial amplitudes and time constants of deactivation. The model differs from the leaky integrate-and-fire neuron in that there is no explicit membrane potential reset, but rather action potentials trigger repolarizing conductances. This kind of neuron model was introduced and extensively used by MacGregor (1987). It was favored over the integrate-and-fire model because examination of recordings of STN neurons showed dramatic changes in the membrane potential at the peak of the AHP during repetitive firing.

*Abstract model*

The abstract STN cell model was a conductance-based model, but did not represent the full membrane conductance and voltage trajectory of action potentials. The spike-triggered conductances were represented using an activation variable that could vary between 0 and 1, and decayed exponentially between threshold crossings. The activation variable for a hyperpolarizing afterconductance is given as

$$n_{AHP}(t) = [n_{AHP}(t_0) + \delta_n]e^{-[(t-t_0)/\tau_n]} \quad (1)$$

in which $n_{AHP}$ is the activation variable for the postspike conductance, $t_0$ is the time of the previous action potential, $\tau_n$ is the time constant of decay of the conductance, and $\delta_n$ is the utilization of the current, that is, the increment in activation variable generated by an action potential. The constraint that $n_{AHP} \leq 1$, in conjunction with $\delta_n$, determined whether the conductance is accumulating during repetitive firing. If $n_{AHP}(t_0) + \delta_n \geq 1$, then the conductance is nonaccumulating, and is reset to the same value, $n_{AHP} = 1$, after each action potential. When the utilization is low, the conductance accumulates at a rate determined by the firing rate, the utilization, and the time constant $\tau_n$. At steady state and constant firing frequency $F$

$$n_{AHP}(t_0) = n_{AHP}[(t_0 + 1)/F] = [n_{AHP}(t_0) + \delta_n]e^{-(1/F\tau_n)}$$

Hence

$$n_{AHP}(t_0) = \frac{\delta_n}{e^{-(1/F\tau_n)} - 1} \quad (2)$$

and

$$n_{AHP}(t) = \frac{\delta_n e^{-[(t-t_0)/\tau_n]}}{1 - e^{-(1/F\tau_n)}} \quad (3)$$

(MacGregor and Sharpless 1973). Activation is limited to a maximum of $n_{AHP} = 1$, and for all cases shown here, the time constant, frequency, and utilization of accumulating currents were constrained to prevent this, that is

$$F < -\frac{1}{\tau_n \ln(1 - \delta_n)} \quad (4)$$

For nonaccumulating currents, after a spike the conductance is reset to the same value, $n_{AHP} = 1$, and

$$n_{AHP}(t) = e^{-[(t-t_0)/\tau_n]} \quad (5)$$

The changes in activation variable for accumulating and nonaccumulating conductances during repetitive activity at constant frequency are shown in Fig. 3, *A* and *B*. It should be noted that the distinction between accumulating and nonaccumulating currents is a matter of utilization of the conductance, not its activation or deactivation rate. Rapidly deactivating conductances may still be accumulating if they are incompletely activated on each spike. In general, the deactivation rate affects the time required for the accumulation to reach steady state (fast deactivation rates are faster to reach steady state at constant firing rate) and the relationship between steady-state accumulated current and firing rate (rapidly deactivating currents accumulate less at all frequencies). This relationship is apparent in the equation for Fig. 3*A*, which shows that the magnitude of steady-state accumulation is a function of the product of firing frequency and deactivation time constant.

As shown by Kernell (1968) and by MacGregor and Sharpless (1973), spike-frequency adaptation in model neurons with a single nonaccumulating AHP conductance is complete by the second action potential, and the *F–I* curves for such model neurons have slopes that increase continuously with frequency, resembling a secondary range (Fig. 3*E*). Model neurons possessing a single accumulating AHP conductance show approximately exponential spike-frequency adaptation resembling that of many neurons including motoneurons and cortical pyramidal cells (e.g., Wang 1998), but do not show a secondary range in the *F–I* curve (Fig. 3*D*). The absence of secondary range firing does not produce any problem for models of cortical pyramidal cells, which generally do not have a steeper *F–I* slope corresponding to secondary range firing, but is an issue to be addressed for spinal cord motoneurons, and of course for neurons of the subthalamic nucleus. Examples showing spike-frequency adaptation and *F–I* curves for a simple model neuron possessing a single AHP conductance of the accumulating or nonaccumulating types are shown in Fig. 3, *D* and *E*. The model neuron used in these very simple simulations was represented by the following current balance equation applied between crossings of the threshold $v_\theta$

$$\frac{dv}{dt} = [I_{app} - \bar{g}_{AHP}n_{AHP}(v - v_o) - g_L(v - v_L)]/C \quad (6)$$

in which $I_{app}$ is applied current, $\bar{g}_{AHP}$ is the maximal AHP conductance, $v_o$ and $v_L$ are the reversal potentials for the AHP and leak currents, respectively, and $n_{AHP}$ is the activation variable of the AHP conductance as defined above. In the model neuron given here, the slopes of the *F–I* curve can be approximated using the assumption that voltage changes more rapidly than n, and so the steady-state solution of *Eq. 6* can be used

$$0 = I_{app} - \bar{g}_{AHP}n_{AHP}(v - v_o) - g_L(v - v_L)$$

$$v = \frac{I_{app}\bar{g}_{AHP}v_o + g_Lv_L}{\bar{g}_{AHP}n_{AHP} + g_L(v - v_L)} \quad (7)$$

The effect of this approximation on the typical trajectory between action potentials in the model neuron is shown in Fig. 3*C*. Substituting the steady-state *Eq. 3* for $n_{AHP}$ into *Eq. 7*, and solving for frequency when $v = v_\theta$ and $t - t_0 = 1/F$, gives the solution of the *F–I* curve in the case of the accumulating AHP

$$F = \frac{1}{\tau_n \ln\left[1 - \frac{\bar{g}_{AHP}\delta_n(v_o - v_\theta)}{I_{app} + g_L(v_L - v_o)}\right]} \quad (8)$$

Changes in leak current translate the *F–I* curve along the $I_{app}$ axis, but do not change its overall form.

We can calculate the slope of the *F–I* curve as a function of frequency instead of current if we substitute *Eq. 3* with $t - t_0 = 1/F$ into *Eq. 7*, differentiate with respect to $I_{app}$, and solve for $dF/dI_{app}$. The resulting equation is

$$\frac{dF}{dI_{app}} = \frac{e^{-(1/F\tau_n)}(1 - e^{1/F\tau_n})^2F^2\tau_n}{\bar{g}_{AHP}\tau_n\delta_n(v_\theta - v_o)} \quad (9)$$

For sufficiently high values of $F$, this gives rise to an asymptotic line (Fig. 3*D*) with slope

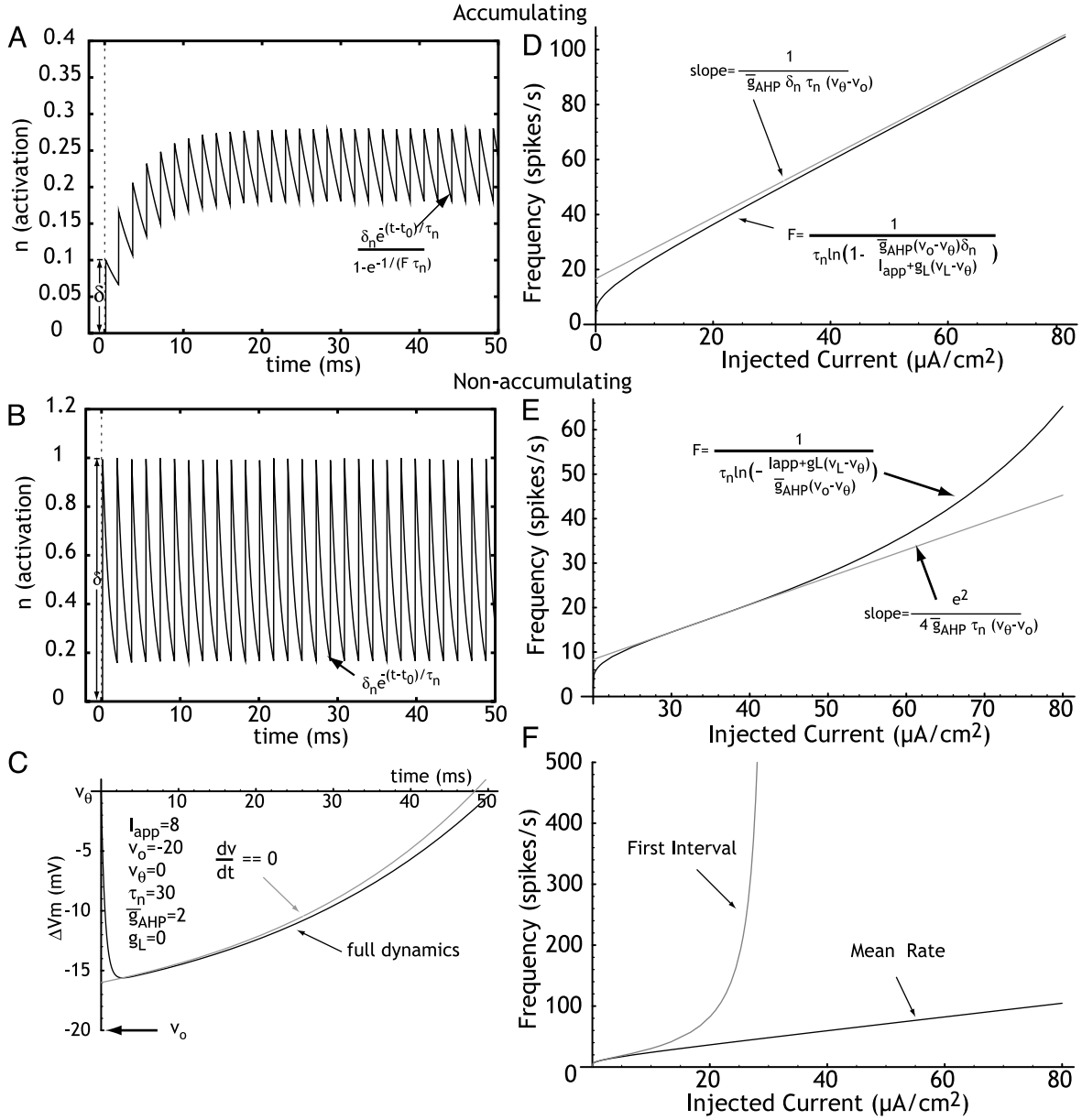


FIG. 3. Abstract model containing a single afterhyperpolarization (AHP) conductance. *A*: accumulation of activation during constant rate repetitive firing for a conductance with small increment δ of activation per spike. *B*: lack of accumulation of activation when the conductance is completely utilized. *C*: effects of the simplification of the abstract model on the interspike voltage threshold at constant frequency of firing. Voltage threshold is set to 0 mV, and the reversal potential for the AHP is −20 mV. Solid line is the solution for the full model (*Eq. 6*). Gray line is the approximation used to obtain *Eq. 7*. Main deviation between the curves is in the first millisecond of firing, and would affect the results only at the highest firing frequencies. *D*: *F–I* curve for the case of a single accumulating conductance. Solid line is the solution from *Eq. 8*. Gray line shows the asymptotic linear *F–I* curve for high frequencies (*Eq. 10*). *E*: *F–I* curve for a single nonaccumulating conductance (*Eq. 11*). *F–I* curve is not linear, but the primary range can be approximated by a straight line drawn through the inflection point at $F = \frac{1}{2}\tau_n$ (*Eq. 13*, gray line). *F*: spike-frequency adaptation in this simple model is indicated by the difference between the *F–I* curves calculated for the steady state in the accumulating model and that for the first interval. Parameters as in *D*.

$$\frac{dF}{dI_{app}} = \frac{1}{\bar{g}_{AHP}\tau_n\delta_n(v_\theta - v_o)} \qquad (10)$$

This linear asymptote is in agreement with a variety of studies on accumulating AHP currents in a variety of neuron models (Ermentrout 1998; Liu and Wang 2001; MacGregor and Sharpless 1973; Wang 1998).

For the nonaccumulating AHP conductance, the solution for frequency is

$$F = \frac{1}{\tau_n \ln\left[-\frac{I_{app} + g_L(v_L - v_\theta)}{\bar{g}_{AHP}(v_o - v_\theta)}\right]} \qquad (11)$$

This *F–I* curve has no linear region, and the slope continuously increases with *F* as the current increases. The reason for this can be appreciated by examination of the interspike membrane potential trajectory in Fig. 3*C*. The trajectory consists of an initial period of slow change (sometimes called the scoop)

followed by a steeper depolarizing portion (the ramp). Although depolarizing current does alter the shape of this trajectory somewhat, the basic scoop and ramp shape remains. Increasing the depolarizing current causes the next action potential to occur earlier, at membrane potentials closer to the scoop portion. The reduced slope of the membrane potential trajectory means that smaller depolarizations will have greater effects on the ISI. At moderate values of $I_{app}$ as shown in Fig. 3*E*, the increasing slope appears similar to the secondary range firing seen in motoneurons and STN neurons. The slope of the *F–I* curve, as a function of frequency, is computed as before. We substitute *Eq. 5* with $t - t_0 = 1/F$ into *Eq. 6*, differentiate with respect to $I_{app}$, and solve for $dF/dI_{app}$ to obtain

$$\frac{dF}{dI_{app}} = \frac{F^2 \tau_n e^{1/F\tau_n}}{\bar{g}_{AHP}(v_\theta - v_o)} \quad (12)$$

Note, from Fig. 3*E*, that the *F–I* curve has one inflection point. This occurs at $F = \frac{1}{2}\tau_n$ and at that point

$$\frac{dF}{dI_{app}} = \frac{e^2}{4\tau_n \bar{g}_{AHP}(v_\theta - v_o)} \quad (13)$$

Spike-frequency adaptation in this model, either with accumulating or nonaccumulating AHP currents, fails to resemble either STN neurons or motoneurons. The difference is especially evident for the STN neurons because this model shows rapid spike frequency adaptation, whereas STN cells exhibit a slow spike frequency increase during repetitive firing in the secondary range. Because there is no adaptation when the AHP current does not accumulate, the degree of spike-frequency adaptation at each level of current can be assessed by comparing the *F–I* curve for the accumulating current at steady state with that of the version with nonaccumulating current (Fig. 3*F*).

### *Combination of accumulating and nonaccumulating AHP conductances*

In many neurons, including subthalamic cells, action potentials trigger a series of conductances with varying time courses. In subthalamic cells, as in motoneurons and cortical pyramidal cells and others, a fast, short-duration AHP is generated by the same currents responsible for repolarization after the action potential. This fast AHP is followed by a slower AHP conductance, part of which is dependent on calcium entry associated with the action potential and which is sensitive to apamin (Bevan and Wilson 1999). In subthalamic cells at least, calcium-dependent $K^+$ currents responsible for at least part of the slower AHP do accumulate during repetitive firing, as one would expect (Bevan and Wilson 1999; Hallworth et al. 2003). It is likely that the faster spike repolarization currents are more completely activated during action potentials. This is because they must activate on a time scale comparable to the action potential, and the action potential achieves depolarizations

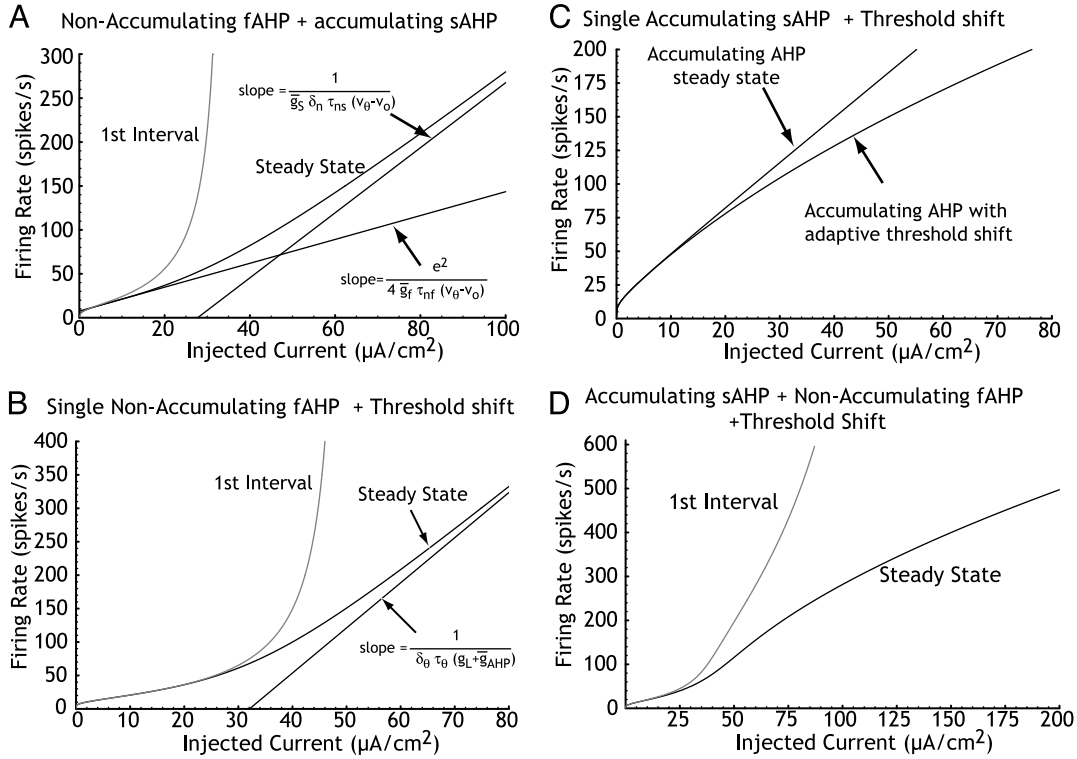


FIG. 4. Combinations of accumulating and nonaccumulating AHP conductances with adaptive threshold shift. *A*: combination of fast nonaccumulating and slow accumulating AHP conductances results in nearly linear primary and secondary firing ranges. Primary range slope is approximately the same as the asymptotic value for the inflection point for the nonaccumulating current alone, and the high-frequency asymptote has the same slope as the asymptotic value for the accumulating current alone (see Fig. 3 and *Eqs. 10* and *13*). *B*: adding the threshold shift to the nonaccumulating model produces a secondary range similar to that obtained with an accumulating AHP, but with a slope determined by the parameters of the threshold shift (*Eq. 19*). *C*: adding accumulating spike-triggered threshold elevation to the accumulating conductance causes it to decelerate at high frequencies. *D*: combination of fast nonaccumulating AHP, slow accumulating AHP, and threshold accommodation produces a sigmoidal steady-state *F–I* curve with primary, secondary, and tertiary ranges, but with pronounced spike-frequency adaptation.

sufficient for nearly complete activation. For example, the utilization of the delayed rectifier current in the squid giant axon is approximately 36% of its maximum during a single action potential (Jack et al. 1975), and approximately 46% of maximal $I_A$ and $I_D$ voltage-sensitive K conductance is attained during an action potential in hippocampal CA3 pyramidal cells (Mitterdorfer and Bean 2002). Although these values seem to leave some headroom for accumulation of AHP conductance, in fact any cumulative effects these can have were shown to necessarily complete within a few ISIs at best (Kernell and Sjöholm 1973). Most models of accumulating AHP conductances have been based on conductances that are activated in only tiny increments on each action potential, such as calcium-dependent potassium conductances.

We combined a rapidly deactivating, nonaccumulating AHP conductance to represent the more completely utilized voltage-sensitive $K^+$ currents, and a smaller, slowly deactivating, accumulating one to determine the interactions of these in generating *F–I* curves and spike-frequency adaptation. The combination produced an *F–I* curve with a pronounced secondary range, as shown in Fig. 4*A*.

The slope of the *F–I* curve for the combination was calculated using the method described above. The model neuron is represented by the current balance equation

$$\frac{dv}{dt} = [I_{app} - \bar{g}_f n_f(v - v_o) - \bar{g}_s n_s(v - v_o) - g_L(v - v_L)]/C \qquad (14)$$

in which $\bar{g}_f$ and $n_f$ describe a faster, nonaccumulating AHP conductance, and $\bar{g}_s$ and $n_s$ describe a slower, accumulating one. Both of these share the reversal potential $v_o$, and the threshold is again $v_\theta$. Because $n_s$ is accumulating and $n_f$ is nonaccumulating, it follows that at steady state

$$n_s(1/F) = \frac{\delta_s}{e^{1/F\tau_s} - 1}$$

and

$$n_f(1/F) = e^{-(1/F\tau_f)} \qquad (15)$$

We assume that $n_s$ and $n_f$ evolve on a slow time scale compared to membrane potential. Hence

$$0 = I_{app} - \bar{g}_f n_f(v - v_o) - \bar{g}_s n_s(v - v_o) - g_L(v - v_L) \qquad (16)$$

We plug *Eq. 15* into *Eq. 16*, differentiate with respect to $I_{app}$, and solve for $dF/dI_{app}$ to find that

$$\frac{dF}{dI_{app}} = \frac{F^2}{\dfrac{\bar{g}_f e^{-(1/F\tau_n)}(v_\theta - v_o)}{\tau_f} + \dfrac{\bar{g}_s e^{1/F\tau_s}(v_\theta - v_o)\delta_s}{(e^{1/F\tau_s} - 1)^2\tau_s}} \qquad (17)$$

For high frequencies, the slope reduces to the same value as that of the single accumulating conductance, whereas at frequencies too low for significant accumulation of the slower AHP it is the same as that for the nonaccumulating conductance. The frequency at which the *F–I* curve changes slope is determined by time constant and utilization of the accumulating current, and its maximal size ($\bar{g}_s$) compared to the nonaccumulating one. Note that addition of an accumulating AHP current did not prevent the occurrence of a change in slope in the *F–I* curve, but linearized the high-frequency portion, making the *F–I* curve appear to be bilinear.

Spike-frequency adaptation in all of these cases occurred primarily in the secondary range. This can be appreciated by comparing the *F–I* curve for the first interval with that of the steady state (Fig. 4*A*). The first interval is entirely determined by the nonaccumulating portions of both currents, and thus has an *F–I* curve similar to that of the fast AHP alone. Spike-frequency adaptation will occur only in the frequency range over which the *F–I* curves for the fast-only and the combined models diverge. The difference between those curves is proportional to the amount of spike-frequency adaptation that occurs at steady state for each frequency.

### *Changes in threshold*

Accumulating AHP currents produce linear *F–I* curves at frequencies below those that drive the accumulating conductance to maximal values. Beyond this, the current is effectively nonaccumulating, and the *F–I* curve slope increases precipitously. Presumably, firing would fail in real neurons at such rates because of spike threshold accommodation. In real subthalamic and other neurons, the voltage threshold for firing increases gradually over time during repetitive firing (e.g., Fig. 1) because of inactivation of inward currents and/or accumulation of outward currents responsible for the threshold. Wang (1998) showed that this phenomenon could produce results similar (but not identical) to the addition of an accumulating AHP conductance. Accumulation of AHP currents are expected to produce a threshold shift over time, because the amount of activation of Na currents required to achieve equality with outward currents must increase, although other factors, including inactivation of sodium currents, are likely to be more influential (Fig. 1*E*). Thus we represented the threshold shift as parametrically independent of the AHP currents, by adding an accumulating activation variable that was responsible for setting the voltage threshold $v_\theta$. For constant firing frequency at steady state

$$v_\theta(1/F) = v_\theta(0) + \frac{\delta_\theta}{e^{1/F\tau_\theta} - 1} \qquad (18)$$

in which $v_\theta(0)$ is the voltage threshold after a long period of inactivity, $\delta_\theta$ is the incremental change in threshold that occurs after each action potential, and $\tau_\theta$ is the time constant of return of threshold to baseline after an action potential. For simplicity, this approach assumes that all change in threshold would occur because of action potentials, and disregards subthreshold accommodative processes. The steady-state threshold versus frequency relation expected from this approximation is compared to the actual steady-state value for a representative STN cell in Fig. 1*D*. The *F–I* curve and adaptation obtained using this model in combination with nonaccumulating and accumulating AHP currents are shown in Fig. 4, *B* and *C*.

Like the combination of fast nonaccumulating and slow accumulating AHP currents, the addition of an adaptive threshold to the nonaccumulating AHP produced spike-frequency adaptation and linearized the *F–I* curves at high frequency without changing repetitive firing at low frequency. The high-frequency asymptotic slope obtained using threshold adaptation was different, however. This slope is computed by substitution of $t - t_0 = 1/F$ (*Eq. 5*) and *Eq. 18* into *Eq. 7*, differentiation of the resulting equation with respect to $I_{app}$, letting $F \rightarrow \infty$, and then solving for $dF/dI_{app}$. It follows that the asymptotic slope is

$$\frac{dF}{dI_{app}} = \frac{1}{\delta_\theta \tau_\theta (g_L + \bar{g}_{AHP})} \quad (19)$$

The result is that when the slope of the *F–I* curve is limited by the threshold shift, the high-frequency asymptotic slope depends on the growth of the threshold and the combined maximal conductances of the leak and the AHP conductance, but not firing frequency or the time constant of the AHP current (Fig. 4*B*). Although the secondary range is linearized as in the case of an added accumulating conductance, the slope is dependent on the parameters of spike threshold change, not outward current.

When the same adaptive change in threshold was combined with the accumulating AHP current, the result was that the slope of the *F–I* curve could be reduced at high frequencies. At sufficiently high frequencies the slope of the *F–I* curve approached zero (Fig. 4*C*).

Adding the threshold change to the model with a fast nonaccumulating and slow accumulating AHP produced *F–I* curves with the appearance of those observed in neurons that show secondary range firing (Fig. 4*D*). The *F–I* curve had a small slope at low frequencies (the primary range), a steeper almost linear region at intermediate frequencies (the secondary range), and a gradual decrease in slope at high frequencies (sometimes called tertiary range). By reducing the strength of the nonaccumulating current (or increasing the strength and/or time constant of the accumulating current) the primary range could be reduced or abolished, yielding an *F–I* curve resembling that seen in cells that do not show secondary range firing (e.g., cortical pyramidal cells). A key result of this is that at steady state, the influences of accumulating currents occur at all frequencies, so that adding another accumulating current with a different time constant does not add an inflection point to the steady-state *F–I* curve, but changes only its slope. Adding more AHP currents reduces the slope of the secondary range, whereas removing them makes the secondary and tertiary ranges steeper. Note this does not fully explain the effects of apamin or ω-conotoxin-GVIA, on subthalamic cells, because these both had profound effects on firing at low frequencies, and of course show reverse spike-frequency adaptation.

The time constants of AHP current accumulation are important for the temporal structure of spike-frequency adaptation (see below), but for purposes of calculating the steady-state frequency, alter only the total accumulation.

### *Reverse spike-frequency adaptation*

The above results indicate that secondary range firing need not arise from the same mechanism that produces firing rate speedup seen in STN neurons, but can arise as well from the mechanisms that produce spike-frequency adaptation. This explains the fact that secondary range firing is seen in spinal cord motoneurons and other cells that do not show speedup during repetitive firing, in the subgroup of STN neurons that do not speed up, and in STN neurons in which speedup has been reduced or abolished by blockade of calcium currents. These mechanisms producing secondary range firing have in common that the fastest AHP conductances are nonaccumulating, but at high frequencies repetitive firing is influenced by accumulating processes that either slow or speed firing. Candidate mechanisms for producing reverse spike-frequency adaptation seen in subthalamic cells must include any inward current that adds to injected current, and that accumulates over the course of the spike train (to explain the gradual nature of the speedup), or the gradual loss of an outward current at high frequencies, perhaps because of inactivation. Either of these will effectively shift the balance of accumulated current in favor of inward current. In the case of an accumulating inward current, it could arise from a spike-generated afterconductance, or could be a subthreshold conductance that is increasingly activated because of a change in the membrane potential trajectory between action potentials. We will consider an inward current that is triggered by action potentials and decays in a voltage-independent manner between spikes.

With the addition of an accumulating ADP conductance, the current balance equation for the simple model is

$$\frac{dv}{dt} = [I_{app} - \bar{g}_f n_f (v - v_o) - \bar{g}_m n_m (v - v_i) - \bar{g}_s n_s (v - v_o) - g_L (v - v_L)]/C \quad (20)$$

in which $\bar{g}_s$ is the maximal conductance for the slow outward current, $n_s$ is its activation variable, and likewise for the medium inward current and the fast outward current. The reversal potential for the inward current is $v_i$. Because $n_s$ and $n_m$ are assumed to be accumulating currents and $n_f$ is nonaccumulating, it follows that at steady state

$$n_f(1/F) = e^{-(1/F\tau_f)} \quad n_m(1/F) = \frac{\delta_m}{e^{1/F\tau_m} - 1} \quad n_s(1/F) = \frac{\delta_s}{e^{1/F\tau_s} - 1} \quad (21)$$

As before, we assume that the conductances evolve on a slow time scale with respect to the membrane potential. Hence

$$0 = I_{app} - \bar{g}_f n_f (v - v_o) - \bar{g}_m n_m (v - v_i) - \bar{g}_s n_s (v - v_o) - g_L (v - v_L) \quad (22)$$

We set $v = v_\theta$, apply *Eq. 21* to *Eq. 22*, and differentiate with respect to $I_{app}$ to find that

$$0 = 1 - \frac{\bar{g}_m (v_\theta - v_i)\delta_m}{F^2 \tau_m [e^{1/F\tau_m} - 1]^2} \frac{dF}{dI_{app}} - \frac{\bar{g}_s (v_\theta - v_o)\delta_s}{F^2 \tau_s [e^{1/F\tau_s} - 1]^2} \frac{dF}{dI_{app}} - \frac{\bar{g}_f (v_\theta - v_o)}{F^2 \tau_f} e^{-(1/F\tau_f)} \frac{dF}{dI_{app}} \quad (23)$$

We now let $F \to \infty$ to find that the asymptotic slope of the secondary range is given by

$$\frac{dF}{dI_{app}} = \frac{1}{\bar{g}_m \delta_m \tau_m (v_\theta - v_i) + \bar{g}_s \delta_s \tau_s (v_\theta - v_o)} \quad (24)$$

At steady state, the slope of the secondary range is determined by a linear combination of the accumulating currents. Because the reversal potential for the accumulating ADP current is positive to threshold and that of the accumulating AHP current is negative to threshold, the sign of these 2 contributions differs. So long as the AHP current(s) exceeds the ADP current (m), the net effect is spike-frequency adaptation, and the slope will be positive. If the current through the inward conductance exceeds that through to the outward conductance, the slope will be negative, and the cell's response will be unstable. This result shows that a steep slope of the secondary range does not imply speedup because it can occur when the net accumulating current is outward. It appears from this, in fact, that at steady state, reverse spike-frequency adaptation is impossible over the parameter range for which cells have a continuous and monotonic *F–I* curve. However, the presence of voltage-sensitive threshold shift can restore stability in the presence of a net inward accumulating current. The *F–I* curve for the

3 spike-triggered conductances combined with an adaptive threshold shift was calculated as described above, and is shown in Fig. 5, *A–D*. The combination of a net inward accumulating current, a fast nonaccumulating AHP conductance, and the frequency-dependent shift in spike threshold can produce a stable monotonic steady-state *F–I* curve even when the net accumulating current is inward. This arrangement can produce reverse spike-frequency adaptation at steady state when the net accumulating current is inward, as indicated by the difference between the steady-state and first-interval *F–I* curves (Fig. 5*A*). Reducing the accumulating AHP in this model produced steeper secondary ranges and transition to secondary range at a lower value of injected current (Fig. 5*B*). Because the maximal rate was limited by the threshold shift, this result did not necessarily produce a change in the maximal firing rate. Proportional reduction of both the inward and outward currents (as expected for blockade of HVA calcium currents) reduced the distinction between primary and secondary ranges (Fig. 5*C*).

### *Time course of speedup*

The approach described above offers solutions only for steady-state firing rate and the rate for the first interval. To obtain information on the temporal evolution of firing rate during the train, the simple threshold model used in the calculations above was simulated using xppaut (B. Ermentrout, Univ. of Pittsburgh). These simulations used the same spike-triggered currents and changes in threshold described above, including a rapidly deactivating nonaccumulating AHP conductance, a slowly deactivating small but accumulating AHP conductance, an adaptive shift in threshold, and a depolarizing spike afterconductance with intermediate size and deactivation time constant. They did not make the simplification of *Eq. 22* (assuming voltage changes are much faster than conductance), but instead included the full dynamics of the simple model. An example showing the changes in firing rate over the course of 1-s current pulses is shown in Fig. 5*E*, using the same parameters used in Fig. 5*A*. The time required for firing to attain steady state was often very long, and it is apparent that in this simulation firing had not completely settled by the end of 1 s. The reason for the long firing rate transients is the long time course of accumulation of AHP and ADP currents. Additionally, the speedup in firing rate was not monotonic, but could (like the transients for STN neurons shown in Fig. 1) be followed by a gradual decrease in firing. This occurred because of the difference in rate of accumulation of inward and outward

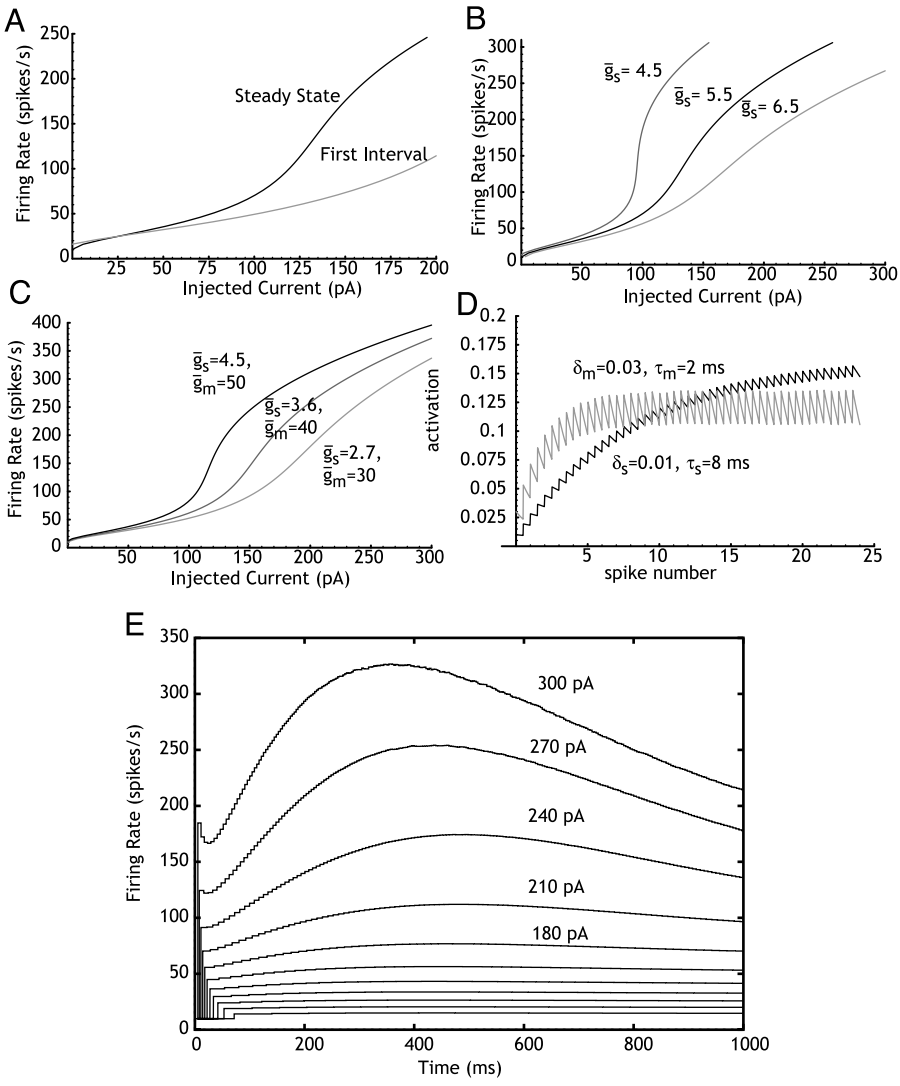


FIG. 5. Addition of medium-duration spike-triggered inward current can control the shape of the secondary range and produce steady state or transient reverse spike-frequency adaptation. *A*: reverse spike-frequency adaptation with addition of an inward current to the model in *D*. *B*: decreases in the strength of the slow AHP conductance ($g_s$) controls the slope of the secondary range, and the current level at which the transition to the secondary range occurs, comparable to the effects of apamin. *C*: proportionate decreases in both the medium afterdepolarization (ADP) ($g_m$) and slow AHP conductances [meant to mimic the effects of high-voltage activated (HVA) calcium current blockers] flattens the secondary range. *D*: because of its more rapid deactivation, the inward current accumulates to its peak earlier, producing a transient period of net spike-generated inward current during the beginning of repetitive firing. *E*: simulation of the evolution of firing rate during repetitive firing for the abstract model. Firing rate increases over the early course of firing, then decays slowly as the slower outward current accumulates. Except where noted, $v_i$ = 40 mV, $v_0$ = −90 mV, $v_L$ = −30 mV, $g_L$ = 0.09 mS/cm$^2$, $\bar{g}_f$ = 7.0 mS/cm$^2$, $\bar{g}_s$ = 5.5 mS/cm$^2$, $\bar{g}_m$ = 40.0 mS/cm$^2$, $\tau_f$ = 30 ms, $\tau_s$ = 500 ms, $\tau_m$ = 150 ms, $\tau_\theta$ = 20 ms, $\delta_m$ = 0.01, $\delta_s$ = 0.01, $\delta_\theta$ = 3, $v_\theta(0)$ = −40 mV.

aftercurrents, as illustrated in Fig. 5*D*. At approximately constant frequency, the larger and more rapidly decaying ADP current increased more rapidly in the beginning of driven firing, but is gradually counteracted by the more gradually accumulating AHP current. The overall time course of this increase and decrease is determined by the difference in deactivation rates (and thus accumulation rates) of the two aftercurrents. If the difference between deactivation time constants of the ADP and AHP conductances is small, the growth and decay of firing rate during driven firing was moderate and slow. Large differences in those time constants caused oscillations of firing rate.

Transient speedup could be observed even when there was no reverse spike-frequency adaptation in the steady-state *F–I* curve. That is, even when the steady-state balance of accumulated current was outward, it was still possible to obtain speedup for the mean rate achieved in response to a current pulse. If the cell approaches steady-state firing slowly, as in the simulations and STN cell recordings, an apparent reverse spike-frequency adaptation is seen with current pulses in the range usually used ($\leq$1 s).

### *A more realistic model of the subthalamic neuron*

To determine whether the above results were consistent with more realistic models of conductances shown to be present in STN neurons, a single-compartment full-spiking model of the STN cell was generated using xppaut. The model was an elaboration of that used by Terman et al. (2002) in their model of the subthalamopallidal network. Action potentials were generated by fast voltage-dependent potassium currents, which also served as the only fast AHP current. HVA calcium currents were generated by a single HVA noninactivating calcium conductance, and the calcium that entered through that conductance controlled the calcium-dependent potassium conductance. Calcium buffering and diffusion were simulated using the mechanism described in Wilson and Callaway (2000). The internal volume of the neuron was represented by 40 concentric shells of equal radial thickness, and the diffusion rate of calcium was controlled by an effective diffusion constant. A noninactivating low-threshold sodium conductance was added (by a window current) to generate spontaneous rhythmic spiking as seen in STN neurons (Bevan and Wilson 1999). The equations for these conductances are given in the METHODS section, and typical values for the parameters are given in Table 1.

Examples showing the driven responses of this model neuron are shown in Fig. 6. Threshold shift in this model occurred mainly because of inactivation of the sodium channel, and no special effort was made to adjust the threshold shift to match that seen in STN neurons. The threshold shift was sufficient,

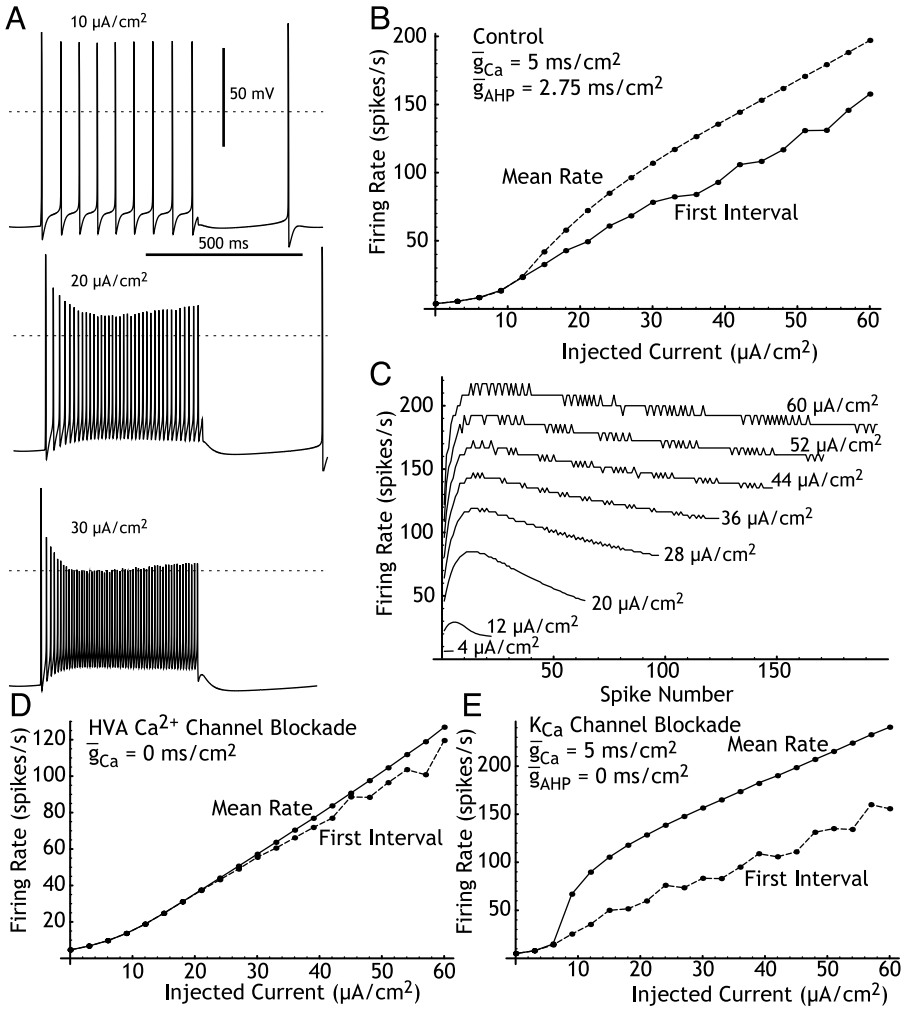


FIG. 6. Results with the more realistic (spiking) model. *A*: firing induced by a 500-ms current pulse. Note adaptive shift in threshold at higher firing rates. *B*: first interval and mean rate *F–I* curves for the response to 1-s current pulses. *C*: evolution of firing rate over the course of a 1-s current pulse at various levels used in the *F–I* curve. *D*: effect of blockade of the calcium current. *E*: effect of blockade of calcium-dependent potassium current. Parameters as in Table 1.

however, to maintain steady-state reverse spike-frequency adaptation without instability of the neuron. Utilization of the fast potassium current was low (about 56% in the simulations shown, resulting in activation of about 10% of maximal $g_k$), but the current did not accumulate. Rather, it decreased somewhat at high frequencies because of reductions in spike amplitude brought on by sodium inactivation (Fig. 7*C*). The lack of accumulation of the fast AHP current was sufficient to create a clear primary range and secondary range firing (Fig. 6*B*, mean rate). Saturation of firing rate at high frequencies was caused by sodium inactivation, and at the highest frequencies firing failed part way through the current pulse, as it did in subthalamic cells (not shown). In addition to showing speedup in mean rate, the model cell exhibited transient increases followed by decreases in firing rate (Fig. 6*C*) as seen in STN neurons. Reductions of calcium-dependent potassium current produced a leftward shift in the secondary range, as seen with apamin blockade in STN neurons (Fig. 6*E*). Blockade of calcium current abolished speedup and greatly decreased the difference in slope between the primary and secondary ranges (Fig. 6*D*). This is as expected from the simple model, and also corresponds in part to the result seen in subthalamic cells with blockade of HVA calcium currents.

The temporal factors responsible for the transient speedup were apparent from examination of activation of individual currents during repetitive firing, as shown in Fig. 7. The fast AHP spike repolarizing conductance showed no accumulation of activation at any rate. Instead, this conductance rapidly decreased during the first spike or 2 of repetitive firing and reached a steady value (Fig. 7*C*). This decrease in activation of the fast AHP current was caused by the reduction in spike amplitude (Fig. 7*A*) as a result of accumulation of sodium inactivation. The slower conductances with very small incremental activation, $g_{AHP}$ and $g_{Ca}$, both accumulated during repetitive firing. The difference in rates of accumulation is caused by the different rates of deactivation of the conductances. The calcium conductance $g_{Ca}$ has a larger incremental increase per spike and a faster deactivation than the calcium-dependent $K^+$ conductance $g_{AHP}$, so it climbs more rapidly and dominates firing early. Its accumulation is responsible for firing rate speedup, and that is a regenerative process, in which $g_{Ca}$ accumulation increases with increases in firing rate. The accumulation of $g_{AHP}$ eventually checks and reverses the process. The net accumulated current at the end of the pulse remains inward, and the cell is still firing faster at the end of the pulse than it did in the first interval. However, the cell is stabilized by the change in spike threshold because of sodium inactivation, as in the simple model.

### *Responses to more realistic inputs*

One caveat to this and other studies of repetitive firing is the artificiality of constant current pulses as stimuli. For most neurons, including STN neurons, natural inputs are never constant, but are constantly fluctuating, and are never currents, but rather conductance changes. For neurons whose repetitive firing is primarily determined by spike-triggered conductances (as in the model presented here), the processes revealed by injecting current pulses will also govern repetitive firing in response to noisy inputs. To begin an examination of more natural stimulation patterns we subjected the model STN cell used in Figs. 6 and 7 to simulated excitatory postsynaptic current (EPSC) stimuli driven by a Poisson process with a variable mean rate. Individual EPSCs were 0.3 mS/cm$^2$ conductance changes with an instantaneous onset and exponential decay with a time constant of 2.5 ms. They had reversal potentials of 0 mV. The amplitude of the EPSC was adjusted to be subthreshold, but not so small as to require high input rates to drive the cell at high levels. High input rates of low-amplitude EPSCs produced responses almost identical to current pulses, and we were interested in the fluctuations of rate that occur when low density random input patterns are able to drive the neuron transiently to high rates of firing. The results of these simulations are shown in Fig. 8. The firing frequency of the model neuron showed a sigmoidal increase with input rate, similar to that seen for constant current (Fig. 8*A*), indi-

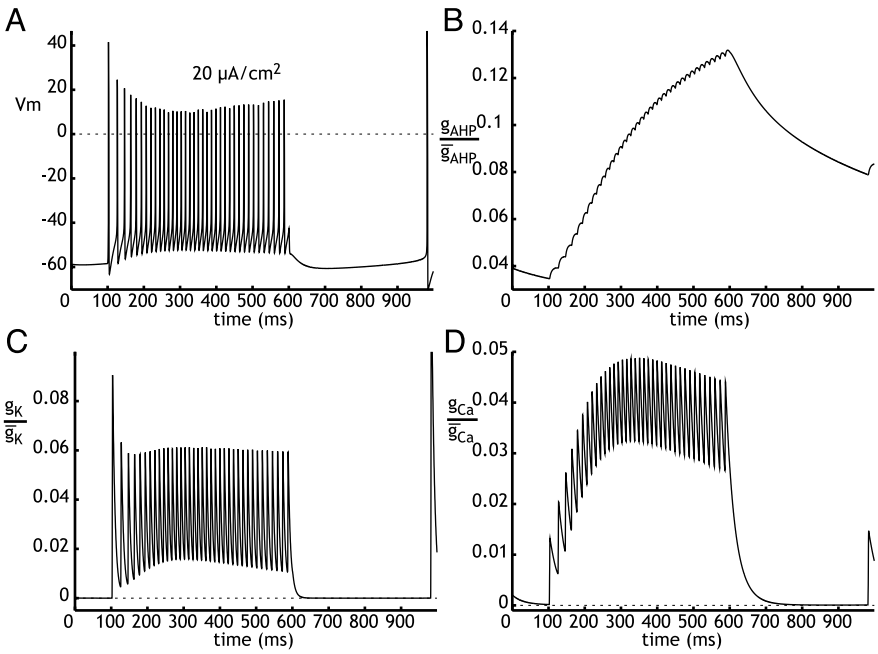


FIG. 7. Changes in conductances of the 3 major spike afterconductances in the more realistic STN model. *A*: episode of driven firing. Note increase in threshold and decrease in spike amplitude caused by inactivation of $Na^+$ conductance. *B*: calcium-dependent potassium current increases slowly, following the intracellular calcium concentration (in the outermost calcium shell). *C*: fast potassium conductance (the delayed rectifier responsible for spike repolarization) is only partly utilized on each spike, but does not accumulate during the train, primarily because of the reduction in action potential amplitude. *D*: calcium conductance triggered by each action potential does accumulate, which causes speedup during the early part of the train.

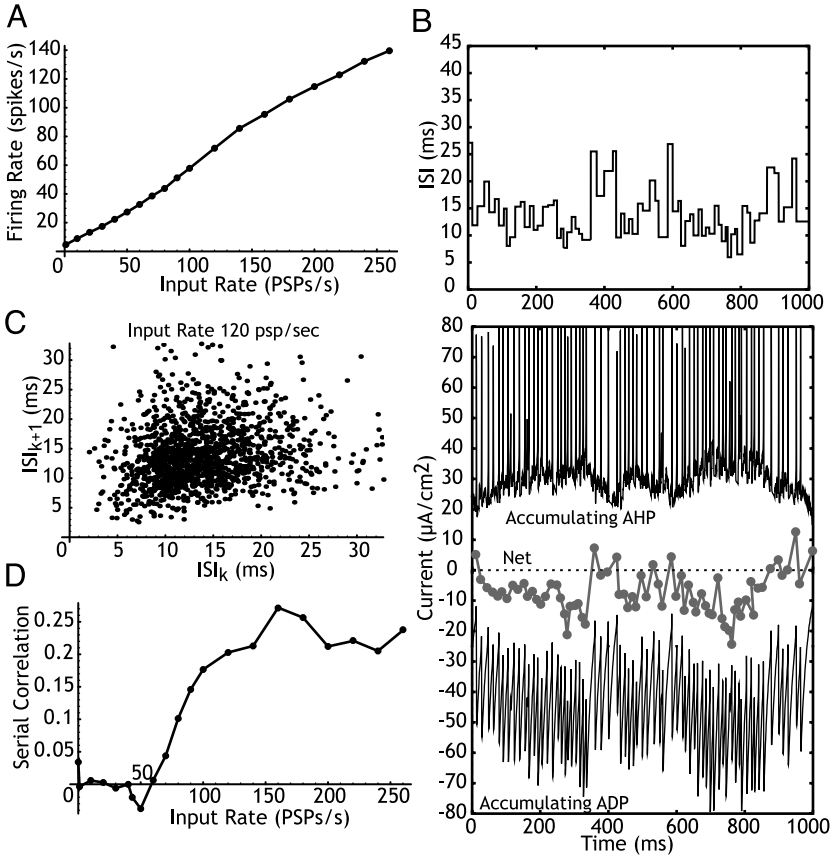


FIG. 8. Activity evoked in the neuron model used in Figs. 6 and 7 by Poisson-driven excitatory postsynaptic current (EPSC) input. *A*: steady-state average neuronal firing rate in response to EPSC inputs at various frequencies. Sigmoidal shape of the rate curve resembles the *F–I* curve (compare with Fig. 6). *B*: fluctuations in firing rate over 1 s of Poisson-driven synaptic activity as indicated by the ISI (*top*). Accumulating AHP and ADP currents fluctuate in parallel with ISI, with ADP currents changing on a faster time scale. Net current is the difference between AHP and ADP currents plotted at times just preceding action potential generation. *C*: serial correlation (first return map) for ISIs at and input rate of 120 input PSCs/s. Correlation at this rate was 0.2. *D*: serial correlation at a range of input rates corresponding to that in *A*. Note that positive correlations develop at firing rates associated with speedup in response to constant current.

cating that the cellular properties responsible for the secondary range are not overwhelmed by the shunting effect of synaptic conductances. Further, cells subjected to irregular synaptic barrage did not achieve a steady-state level of accumulated AHP and ADP conductance, but rather these fluctuated with firing rate. These fluctuations altered the cells' excitability in response to subsequent EPSCs, and this produced correlations in the output pattern of the neurons that were not present in the input pattern. One second of simulation with 120 EPSCs/s input is shown in Fig. 8*B*. The *top graph* shows the fluctuations in ISI of the model neuron generated by the random input pattern over 1 s of activity. Below this are shown the accumulating AHP current, the accumulating ADP current, and the difference between these. The same mechanisms that governed speedup and spike frequency adaptation during constant current pulses act on a spike-by-spike basis to control the excitability of the cell when subjected to a fluctuating drive. At periods of slow firing (long ISI), the ADP current decays more rapidly than the AHP current, and the net accumulated current over the next ISI is outward, reducing cell excitability. During periods of increased PSP density and resulting short ISIs, the ADP current increases more rapidly than the AHP, and the net accumulating current becomes inward. Whether the average of accumulated current over time is net inward or outward is dependent on the average firing rate and the decay time constants of the AHP and ADP conductances. At low rates (those associated with adaptation during constant current injection) the average current is outward, whereas at higher rates the ADP current is dominant at higher frequencies. These spike-generated currents produce a structure on the neuron's spike train, which can be seen as a correlation between adjacent ISIs, as reported by Liu and Wang (2001). Except at very low rates, for which adaptation is dominant, the net effect of the spike-triggered conductances is a positive correlation among adjacent intervals. An example is shown in Fig. 8*C*. The dependency of serial correlation on input rate is shown in Fig. 8*D*, and it can be seen that in the secondary range the serial correlation increases sharply then remains approximately constant.

## DISCUSSION

The approach we have used here follows the approach pioneered by Kernell (1968, 1973) and MacGregor and Sharpless (1972). Those authors showed that nonaccumulating AHPs produce accelerating *F–I* curves that roughly resemble the primary and secondary firing ranges of motoneurons (although the secondary range is not linear), and that accumulating AHPs produce linear *F–I* curves. Kernell (1973) further showed that a combination of a fast nonaccumulating AHP and a slow accumulating AHP and accommodative threshold increases resulting from $Na^+$ inactivation could produce *F–I* curves and adaptation similar to those of motoneurons. For these studies, Kernell used a modified Frankenhaeuser and Huxley model and, with the limited computational resources available at the time, was able to explore the dependency of these phenomena on some but not all of the parameters of the model. Although it is often possible to construct a realistic conductance-based model that reproduces the available experimental data, even today the complexity of the model sometimes makes it difficult to determine the principles that govern the model's activity.

More recently, some investigators (Ermentrout 1998; Liu

and Wang 2001; Wang 1998) have taken a more analytical approach using more simplified models. Liu and Wang (2001) used an integrate-and-fire model to explore spike frequency adaptation and linearization of the *F–I* curve by accumulating AHPs and accommodative threshold changes in the cortical pyramidal cell. The work we present here includes an extension of the work by Liu and Wang (2001), using a steady-state approximation to a MacGregor-style neuron model (MacGregor 1987), which has most of the benefits of the integrate-and-fire model but without the use of an explicit membrane potential reset. Instead, the abstract model allows postfiring membrane potential to evolve in response to the spike-triggered conductances. We included the 4 kinds of postspike influences that were included in the Kernell (1973) model, and which are normally postulated to play a role in repetitive firing. These were represented in a general way that does not assume much about their biophysical mechanisms. The simplifications that were made in the model are *1*) all of the currents were spike-triggered, i.e., they are HVA currents that are not significantly activated by the interspike membrane potential trajectory; *2*) all the currents decayed exponentially after an action potential, i.e., their deactivation time constants were not significantly sensitive to the membrane potential changes that occur between spikes; and *3*) spike threshold changes were spike-triggered, i.e., spike threshold is not significantly affected by the interspike membrane potential trajectory. None of these simplifications is expected to be strictly correct, but at least for subthalamic cells we have shown that they are reasonable approximations.

We show that (as concluded by Kernell 1973), nonaccumulating fast AHP conductances produce accelerating *F–I* curves in the absence of other influences, and that the presence of a nonaccumulating fast AHP is essential for the presence of distinct primary and secondary firing ranges. We further show that the transition between the primary and secondary firing ranges occurs at a frequency largely determined by the ratio of strengths of nonaccumulating and accumulating spike afterconductances. Adding an accumulating ADP to the accumulating AHP conductance changes the slope of the secondary range in the steady-state *F–I* curve, but does not affect its linearity. The slope of the steady-state (postadaptation) primary range is proportional to the reciprocal of the product of the conductance underlying the nonaccumulating AHP, the time constant of its decay, and the difference between its reversal potential and spike threshold. The slope of the secondary range is the reciprocal of the product of the incremental conductance (per spike), the time constant of decay, and the difference between the reversal potential and spike threshold for the accumulating conductances. If there is more than one such conductance, the slope of the steady-state *F–I* secondary range is approximately the reciprocal of the sum of such products for each conductance. In a model with constant threshold, the steady-state *F–I* curve is translated to the left and right by changes in voltage-insensitive (leak) conductances, but these do not alter the slopes of either firing range. Because they do not have an opportunity to accumulate over the first interval, the accumulating conductances have a small effect on the *F–I* curve calculated for the first interval, and so it is accelerated in the fashion of that of nonaccumulating conductances. This model shows spike-frequency adaptation to a greater or lesser extent, but can never exhibit reverse spike-frequency adaptation at steady state. This is because increasing the strength of the ADP current, so that it exceeds the accumulated AHP current at steady state, causes frequency of the cell model to lose stability (the secondary range slope becomes negative).

It should be noted that the model does not perfectly reproduce the repetitive firing of STN neurons. In particular, the effects of apamin blockade of SK channels and of ω-conotoxin-GVIA blockade of $Ca_v2.2$ (N-type) channels produce much larger changes in the primary firing range than predicted by the model. This occurs in the model because, in the primary range, accumulating conductances are too small to influence repetitive firing. If we adjust the per-spike increment or time constant of the accumulating conductances so that they do influence primary range firing in the model, they will saturate at firing rates in the secondary range. It is possible that in subthalamic cells accumulation of these conductances is not linear, and that the per-spike increment of the conductance decreases at high rates. Although this would account for the difference between the model and the neuron, there are other possible explanations and at this time there are not experimental data that can be applied.

The stabilizing influence of adaptive frequency-dependent threshold increases to this model made possible the negative spike-frequency adaptation as seen in subthalamic neurons, in addition to its contributions to the slope of the secondary range and the saturation of firing rate at high currents (tertiary range). Because the contribution of threshold adaptation to the slope of the *F–I* curve depends on total cell conductance, leak conductances can contribute to the slope of the secondary and tertiary firing range by their effects on threshold. The stabilization of firing at high rates produced by threshold changes adds to that of accumulating AHPs, making possible much larger ADP conductances without destabilizing the firing rate. Thus threshold shift is essential for stable steady-state reverse spike-frequency adaptation, which occurs when the ADP current exceeds that of the AHP. Transient speedup and apparent reverse spike-frequency adaptation (when measured from the transient) occurred even when the net accumulating current at steady state is outward. This produces no reverse spike-frequency adaptation in the steady state *F–I* curve, but can produce the appearance of reverse spike-frequency adaptation if the *F–I* curve is obtained for current pulses comparable in duration to the rate transient.

### *Biophysical origin of the ADP and AHP conductances*

The brief, nonaccumulating AHP conductance in most cells arises from the simultaneous activation of a number of different HVA $K^+$ currents. Fast nonaccumulating AHP currents are part of the spike repolarization process. These include the currents normally called delayed rectifiers, and various slow and fast transient potassium currents. Even though they are not fully utilized, they do not accumulate, largely because of their involvement in the spike mechanism. If they get smaller or larger, the spike itself changes in the opposite direction, which changes their subsequent activation (Jack et al. 1975; Kernell 1973). A good example of this is evident in the model shown in Fig. 7*C*. In that simulation, the fast $K^+$ current responsible for spike repolarization and fast afterhyperpolarization is only partly utilized, but fails to accumulate, even at high frequency, and often decreases in strength because of reductions in the

amplitude of the action potential. An interesting possibility not explored in our simulations is the possibility that accumulating inactivation of transient $K^+$ currents could contribute to speedup in STN neurons by reducing the fast AHP. This was not pursued because it predicts that the primary range would be altered over the course of speedup, which is not generally seen (the difference between the first-interval and the steady-state *F–I* curves is usually much greater in the secondary range).

There are also a number of voltage-dependent $K^+$ currents that could accumulate and contribute to the accumulating part of the AHP. One example is the slowly activating persistent $K^+$ current seen, for example, in striatal spiny neurons (Nisenbaum et al. 1996). This sort of current activates a little during the action potential because its time constant of activation is so long, but the small incremental activation it experiences per spike deactivates slowly, so it can accumulate. M-current is also sometimes advanced as a candidate for slow accumulating AHP current (Ermentrout et al. 2001). Other candidates are conductances that accumulate because they are activated by the action of an intracellular messenger whose concentration is incrementally increased by action potentials. The best-known examples of this are calcium-dependent $K^+$ currents, and the calcium-dependent SK current is almost certainly a major contributor to the accumulating AHP in STN neurons (Hallworth et al. 2003). The importance of SK conductance in subthalamic cells is reinforced by the effect of the SK blocker apamin on the *F–I* curves shown in Fig. 2, which is reproduced in the model by reduction of the accumulating AHP conductance. However, complete block of accumulating AHP conductances in the model produced much more dramatic effects, and it is unlikely that SK is the only accumulating AHP conductance in subthalamic cells.

### *Accumulating ADP conductances*

ADP currents have been observed in many neurons, including spinal motoneurons, and there have been a number of different mechanisms proposed. To function as observed in our simulations, an ADP conductance would have to share the same properties as the accumulating AHP conductances. That is, it would be activated by large depolarizations and should be only slightly utilized by single-action potentials, allowing it to accumulate. For it to accumulate, it is not necessary for the ADP current to have a long deactivation time constant. However, the time constant of the ADP conductance is important in determining its properties. We have assumed a time course of deactivation intermediate between the fast and slow AHP conductance (for the neuron in Figs. 6 and 7, the ADP conductance deactivated with a time constant of about 30 ms at −50 mV). This is partly to ensure that the conductance can enhance the inflection between the fast and slow AHP (as observed). Also, if the ADP conductance is too rapidly deactivating, it will accumulate too rapidly, and the cell will rhythmically generate bursts that are terminated by the subsequent accumulation of the AHP conductance. In selecting the ADP deactivation time constant, we were guided by our measurements of spike-triggered calcium transients in STN neurons (Hallworth et al. 2003). Using calcium imaging, we observed somatic calcium transients whose rising phase outlasted action potentials and the initial AHP by 10–50 ms (Hallworth et al. 2003). In the same study, we observed an inward tail current with a similar time course after short, large-amplitude depolarizing voltage-clamp pulses, which was revealed after blockade of SK current with apamin. We are aware that deactivation of HVA calcium channels is usually much faster than this. Measurements of deactivation time constants of calcium currents are not available from the studies in STN neurons (Sidach and Mintz 2002; Song et al. 2000), but have been made for a variety of other cells, and the time constant we have used is longer than usually expected (e.g., Brown et al. 1993). Likewise, in their study of dissociated subthalamic neurons, Do and Bean (2003) measured the cobalt-sensitive component of current evoked by voltage-clamped action potentials, and it was of short duration, being effectively over within 5 ms or so after the action potential. These observations raise some doubt that spike-triggered HVA calcium currents could be solely responsible for the ADP current, despite our observation that blockers of $Ca_v1.2$–1.3 (L) or $Ca_v2.2$ (N) channels often reduced or abolished speedup and reduced the slope of the secondary range of the *F–I* curve, which suggest some role for these channels. A contribution of dendritic currents, not included in our model, may also help to account for this discrepancy. Our findings do not rule out a contribution from other sources, including resurgent $Na^+$ currents, which have been demonstrated to follow action potentials in subthalamic cells (Do and Bean 2003), or calcium-dependent cation current (which would have the appropriate time course but has not yet been described for subthalamic cells).

It should be noted that blockade of $Ca^{2+}$ currents with cadmium produced somewhat different effects on firing in STN neurons than did blockade of specific HVA $Ca^{2+}$ conductances. Cadmium treatment did abolish speedup as expected, but it also produced a large leftward shift in the *F–I* curve, effectively abolishing the primary firing range. This effect of cadmium is reproduced in our model only by reducing the strength of the nonaccumulating fast AHPs. Cadmium has been reported to interfere with inactivating fast $K^+$ currents in some neurons by shifting their inactivation curves (Song et al. 1998). Perhaps this effect of cadmium is responsible for part of the effects seen in STN neurons.

### *Adaptive threshold change*

It has long been acknowledged that changes in spike threshold contribute to regulation of repetitive firing in many neurons. In STN neurons, as in many other cells, accumulation of inactivation of sodium current is a major contributor to spike threshold shifts (Fig. 1). Much of the inactivation responsible occurs during the action potential itself, and so can be treated as spike triggered, as done here, but some occurs in the subthreshold trajectory of the membrane potential. At very low firing rates, we observed a substantial deviation of thresholds from that predicted by an adaptive mechanism (Fig. 1*D*), which is expected because subthreshold $Na^+$ inactivation should be most influential at low firing rates (when the membrane potential approaches threshold most gradually). Another deviation from the model occurred at high rates, presumably because of reduced removal of inactivation during the ISI as the average membrane potential became more positive. Our abstract model did not represent the interaction expected to exist between threshold shift and spike afterconductances. This interaction should occur because the accumulating afterconductances con-

tribute to the overall current balance that determines the spike threshold. Thus accumulation of outward currents should tend to raise threshold, whereas accumulation of inward currents will lower it. These simplifications alter the *F–I* curve at very low and high firing rates, but their effect was not very large, as judged from the results with the more realistic model shown in Fig. 6.

### *Subthreshold currents*

The abstract model described here used strictly spike-triggered conductances. There may be subthreshold-activated currents that contribute directly to speedup and the *F–I* curve. For example, STN neurons have a substantial subthreshold activation of persistent $Na^+$ current that contributes to their spontaneous firing (Beurrier 2000; Bevan and Wilson 1999; Do and Bean 2003). Because this current is relatively fast (compared to the ISI at all rates), it will not accumulate (and will not contribute to speedup) if the threshold and AHP amplitude were fixed. When threshold shift is allowed, it is possible that this current could participate, because its average activation will increase as the average membrane potential is more depolarized. This kind of mechanism (but a calcium current) was proposed by Schwindt and Crill to participate in the secondary range firing of spinal motoneurons (Schwindt and Crill 1982). The effectiveness of this mechanism is mitigated somewhat by the fact that an increased activation of persistent $Na^+$ will tend to counteract the threshold change that causes it (by adding to the total inward current lowering threshold). In the realistic model shown in Fig. 6, the persistent sodium current was present, and we have observed that it can contribute to speedup to some degree. Intermediate between subthreshold and spike-triggered currents are mechanisms like the one responsible for speedup in thalamic reticular cells (e.g., Destexhe et al. 1996). In these cells, dendritic low-threshold calcium conductances contribute to the gradually increasing firing rate seen in those cells during bursts.

### *Functional implications*

The processes that govern spike-frequency adaptation in response to current pulses also determine the responsiveness of neurons to patterns of synaptic activation. Wang (1998) and Liu and Wang (2001) emphasized the role of spike-frequency adaptation in performing a temporal decorrelation of activity in individual neurons under more natural stimulation conditions. Decorrelation induced by spike-frequency adaptation has a time window comparable to that of the conductance change responsible for spike-frequency adaptation. At very low firing rates, at which the afterconductances of action potentials usually have the opportunity to dissipate before the cell is excited again, spikes occur independently of each other. At higher input rates, they show that when the cell is driven to fire a pair of spikes or more at a high rate, adaptive currents accumulate and tend to delay subsequent action potentials, making the cell transiently less responsive. This negative correlation could cause spike trains to be more variable than they would otherwise be, and to cause interference between responses to temporally adjacent stimuli. In general, we have found reverse spike-frequency adaptation to produce the opposite effects. It should enhance the differences between responsive and unresponsive cells over time, and allow cooperative effects between strong and weak stimuli. These influences are wholly predictable from the response to constant current pulses, but under realistic conditions when firing does not remain constant, the cellular mechanisms responsible for spike-frequency adaptation and its inverse exercise a fluctuating spike-by-spike influence on the excitability of the cell. For STN neurons, the result tunes the cells responsiveness to favor nonsynchronous but temporally clustered inputs with a time course several times longer than the duration of the spike-triggered conductances that cause them.

GRANTS

This work was supported by National Institute of Neurological Disorders and Stroke Grants NS-047085 to C. J. Wilson and M. D. Bevan, NS-41280 to M. D. Bevan, and National Science Foundation Grant DMS-0103922 to D. Terman.

REFERENCES

**Baranauskas G, Tkatch T, Nagata K, Yeh JZ, and Surmeier DJ.** Kv3.4 subunits enhance the repolarizing efficiency of Kv3.1 channels in fast-spiking neurons. *Nat Neurosci* 6: 258–266, 2003.

**Beurrier C, Bioulac B, and Hammond C.** Slowly inactivating sodium current (I(NaP)) underlies single-spike activity in rat subthalamic neurons. *J Neurophysiol* 83: 1951–1957, 2000.

**Beurrier C, Congar P, Bioulac B, and Hammond C.** Subthalamic nucleus neurons switch from single-spike activity to burst-firing mode. *J Neurosci* 19: 599–609, 1999.

**Bevan MD, Magill PJ, Hallworth NE, Bolam JP, and Wilson CJ.** Regulation of the timing and pattern of action potentials in rat subthalamic neurons in vitro by GABA-A IPSPs. *J Neurophysiol* 87: 1348–1362, 2002.

**Bevan MD and Wilson CJ.** Mechanisms underlying spontaneous oscillation and rhythmic firing in rat subthalamic neurons. *J Neurosci* 19: 7617–7628, 1999.

**Bevan MD, Wilson CJ, Bolam JP, and Magill PJ.** Equilibrium potential of $GABA_A$ current and implications for rebound burst firing in rat subthalamic neurons in vitro. *J Neurophysiol* 83: 3169–3172, 2000.

**Brown AM, Schwindt PC, and Crill WE.** Voltage dependence and activation kinetics of pharmacologically defined components of the high-threshold calcium current in rat neocortical neurons. *J Neurophysiol* 70: 1530–1543, 1993.

**Cheruel F, Dormont JF, and Farin D.** Activity of neurons of the subthalamic nucleus in relation to motor performance in the cat. *Exp Brain Res* 108: 206–220, 1996.

**Destexhe A, Contreras D, Steriade M, Sejnowski TJ, and Huguenard JR.** In vivo, in vitro and computational analysis of dendritic calcium currents in thalamic reticular neurons. *J Neurosci* 16: 169–185, 1996.

**Do MTH and Bean BP.** Subthreshold sodium currents and pacemaking of subthalamic neurons: modulation by slow inactivation. *Neuron* 39: 109–120, 2003.

**Ermentrout GB.** Linearization of F-I curves by adaptation. *Neural Comput* 10: 1721–1729, 1998.

**Ermentrout GB, Pascal M, and Gutkin B.** The effects of spike frequency adaptation and negative feedback on the synchronization of neural oscillators. *Neural Comput* 13: 1285–1310, 2001.

**Granit R, Kernell D, and Shortess GK.** Quantitative aspects of repetitive firing of mammalian motoneurons caused by injected currents. *J Physiol* 168: 911–931, 1963.

**Hallworth NE, Wilson CJ, and Bevan MD.** Apamin-sensitive SK calcium dependent potassium channels, through their selective coupling to calcium channels, are critical determinants of the precision, pace and pattern of action potential generation in rat subthalamic nucleus neurons in vitro. *J Neurosci* 23: 7525–7542, 2003.

**Jack JJB, Noble D, and Tsein RW.** *Electric Current Flow in Excitable Cells.* London: Oxford Univ. Press, 1975.

**Kernell D.** The adaptation and the relationship between discharge frequency and current strength of cat lumbosacral motoneurons stimulated by long-lasting injected currents. *Acta Physiol Scand* 65: 87–199, 1965.

**Kernell D.** The repetitive impulse discharge of a simple neurone model compared to that of spinal motoneurons. *Brain Res* 11: 685–687, 1968.

**Kernell D and Sjöholm H.** Repetitive impulse firing: comparisons between neurone models based on "voltage clamp equations" and spinal motoneurons. *Acta Physiol Scand* 87: 40–56, 1973.

**Liu Y-H and Wang X-J.** Spike-frequency adaptation of a generalized leaky integrate-and-fire model neuron. *J Comput Neurosci* 10: 25–45, 2001.

**MacGregor RJ.** *Neural and Brain Modeling.* San Diego, CA: Academic Press, 1987.

**MacGregor RJ and Sharpless SK.** Repetitive discharge rate of a simple neuron model with accumulation of after-hyperpolarization conductance. *Brain Res* 64: 387–390, 1973.

**Mitterdorfer J and Bean BP.** Potassium currents during the action potential of hippocampal CA3 neurons. *J Neurosci* 68: 1373–1383, 2002.

**Nisenbaum ES, Wilson CJ, Foehring RC, and Surmeier DJ.** Isolation and characterization of a persistent current in neostriatal neurons. *J Neurophysiol* 76: 1180–1194, 1996.

**Schwindt PC.** Membrane potential trajectories underlying motoneuron rhythmic firing at high rates. *J Neurophysiol* 36: 434–449, 1973.

**Schwindt PC and Crill WE.** Factors influencing motoneuron rhythmic firing: results from a voltage-clamp study. *J Neurophysiol* 48: 875–890, 1982.

**Sidach GS and Mintz IM.** Low-affinity blockade of neuronal N-type Ca channels by the spider toxin ω-agatoxin-IVA. *J Neurosci* 20: 7174–7182, 2000.

**Song WJ, Baba Y, Otsuka T, and Murakami F.** Characterization of Ca(2+) channels in rat subthalamic nucleus neurons. *J Neurophysiol* 84: 2630–2637, 2000.

**Song WJ, Tkatch T, Baranauskas G, Ichinohe N, Kitai ST, and Surmeier DJ.** Somatodendritic depolarization-activated potassium currents in rat neostriatal cholinergic interneurons are predominantly of the A type and attributable to coexpression of Kv4.2 and Kv4.1 subunits. *J Neurosci* 18: 3124–3137, 1998.

**Terman D, Rubin JE, Yew AC, and Wilson CJ.** Activity patterns in a model for the subthalamopallidal network of the basal ganglia. *J Neurosci* 22: 2963–2976, 2002.

**Wang X-J.** Calcium coding and adaptive temporal computation in cortical pyramidal neurons. *J Neurophysiol* 79: 1549–1566, 1998.

**Wichmann T, Bergman H, and DeLong MR.** The primate subthalamic nucleus. I. Functional properties in intact animals. *J Neurophysiol* 72: 494–506, 1994.

**Wigmore MA and Lacey MG.** A Kv3-like persistent, outwardly rectifying CS+-permeable, K+ current in rat subthalamic neurons. *J Physiol* 527: 493–506, 2000.